Atypical chemoreceptor arrays accommodate high membrane curvature

Alise R. Muok[1], Davi R. Ortega[2,3], Kurni Kurniyati[4], Wen Yang[1], Adam Sidi Mabrouk[1], Chunhao Li[4], Brian R. Crane[5], Ariane Briegel[1*]

[1]Institute for Biology, Leiden University, Sylviusweg 72, 2333 BE Leiden

[2]Department of Biology, California Institute of Technology, 1200 E. California Blvd., Pasadena, CA 91125, USA

[3]Laboratory for Research in Complex Systems, 425 California St., Suite 1200, San Francisco, CA 94104, USA

[4]Department of Oral and Craniofacial Molecular Biology, Philips Research Institute for Oral Health, Virginia Commonwealth University, Richmond, VA 23298

[5]Department of Chemistry and Chemical Biology, Cornell University, Ithaca, NY 14850

Abstract/Summary

The prokaryotic chemotaxis system is arguably the best-understood signaling pathway in biology, but most insights have been obtained from only a few model organisms and many studies have relied on artificial systems that alter membrane curvature[1–3]. In all previously described species, chemoreceptors organize with the histidine kinase (CheA) and coupling protein (CheW) into a hexagonal (P6 symmetry) extended array that is considered universal among archaea and bacteria[4,5]. Here, for the first time, we report an alternative symmetry (P2) of the chemotaxis apparatus that emerges from a strict linear organization of CheA in *Treponema denticola* cells, which possesses arrays with the highest native curvature investigated thus far. Using cryo-ET, we reveal that the *Td* chemoreceptor arrays assume a truly unusual arrangement of the supra-molecular protein assembly that has likely evolved to accommodate the high membrane curvature. The arrays have several additional atypical features, such as an extended dimerization domain of CheA and a variant CheW-CheR-like fusion protein that is critical for maintaining an ordered chemosensory apparatus in an extremely curved cell. Furthermore, the previously characterized *Td* oxygen sensor ODP influences array integrity and its loss substantially orders CheA. These results suggest a greater diversity of the chemotaxis signaling system than previously thought and demonstrate the importance of examining transmembrane systems *in vivo* to retain native

30 membrane curvature.

31

32 **Introduction**

33 Chemotaxis is a behavior most motile bacteria employ to sense their chemical environment
34 and navigate toward favorable conditions. The main components of the system are
35 transmembrane chemotaxis receptors called methyl-accepting chemotaxis proteins (MCPs),
36 the histidine kinase CheA, and the adaptor protein CheW. The intracellular tips of MCPs
37 bind CheA and CheW and communicate changes from the external chemical environment
38 into the cell by modulating CheA kinase activity (Fig. S1A)[6–8]. Activation of CheA initiates an
39 intracellular phosphorelay that ultimately controls flagellar rotation and cell movement.
40 CheA functions as a dimer and possesses five domains (P1-P5) with distinct roles in
41 autophosphorylation and array integration. The P1 domain is the phosphate substrate
42 domain, P2 interacts with response regulators, P3 is the dimerization domain, P4 binds ATP,
43 and P5 interacts with CheW. In the model species *Escherichia coli* (*Ec*), CheA P5 and CheW
44 are paralogs that interact pseudo-symmetrically to form six-subunit rings. In all bacterial and
45 archaeal species examined thus far, the MCPs are arranged in a trimer-of-dimer oligomeric
46 state and further organize into a hexagonal lattice (Fig. S1B). In *Ec*, the receptors are
47 connected by the highly ordered rings of CheA and CheW bound to the cytoplasmic tips of
48 the receptors[5,9]. These insights have established a widely accepted central model of the
49 chemotaxis array (Fig. S1B)[4,5,10]. However, emerging research has recently revealed
50 divergent components and arrangements of the chemotaxis apparatus in non-canonical
51 organisms. For example, in *Vibrio cholerae* (*Vc*) chemotaxis arrays, CheA and CheW lack
52 an ordered arrangement in the rings[1,11].

53

54 Many of these structural insights have transpired from cryo-electron tomography (cryo-ET)
55 studies that utilize artificial systems for higher resolution data. Specifically, the advent of so-
56 called 'mini-cell' bacterial strains produce extremely small cells that are ideal for cryo-ET[1,3],
57 and lipid-templating methods generate *in vitro* arrays with increased conformational

58 homogeneity[2,12]. However, these methods generate arrays with non-native curvature and it
59 is unclear how this may affect array structure and behavior. Here, we examine the *in vivo*
60 array structure of the pathogenic spirochete *Treponema denticola* (*Td*) by cryo-ET, which
61 possesses the highest native membrane curvature of any bacteria examined for their
62 chemotaxis system so far[4,5]. We demonstrate the presence of a novel array architecture with
63 two-fold (P2) symmetry in *Td*, that likely owes to the high curvature of the cells. Genetics
64 experiments, bioinformatics analyses, structural investigations, and molecular modeling of
65 *Td* chemotaxis proteins reveals adaptations that have likely evolved to accommodate
66 formation of an extended chemotaxis array in a highly curved membrane. We demonstrate
67 that a CheR-like fusion domain in a variant CheW is key for maintaining the structural
68 integrity of the arrays. Furthermore, cryo-ET analysis of *Td* cells lacking the oxygen sensor
69 ODP reveals substantial changes to the ordering or mobility of CheA[13]. Collectively, these
70 data demonstrate a greater diversity of the chemotaxis system than previously assumed,
71 and exemplify the importance of examining biological structures in native *in vivo* conditions.
72

73 **Results**

74 **Conservation of the F2 chemotaxis system**

75 The chemotaxis systems in prokaryotes have been classified into 19 systems based on
76 phylogenomic markers[14]. These classes include 17 'Flagellar' systems (F), one 'Alternative
77 Cellular Function' system (ACF), and one 'Type Four Pilus system' (TFP). The spirochete
78 chemotaxis system belongs to the 'Flagella class 2' (F2) category, which has not been
79 investigated with structural methods[14]. To explore the characteristics of chemotaxis proteins
80 in F2 genomes, we analyzed genomes in the Microbial Signal Transduction Database
81 version 3 (MiST3)[15]. All genomes (306) with at least one CheA of the F2 class (CheA-F2)
82 are in the Spirochaetota phylum, with a few exceptions of lateral gene transfer to other phyla
83 (Dataset 1, see Supplementary Methods). Not all Spirochaetota bacteria possess an F2
84 system however. There are 1096 genomes assigned to the Spirochaetota phylum in GTDB[16]
85 and 804 of these are present in the MiST3 database (Dataset 2)[15]. With these 804 genomes,

86 we mapped the different classes of CheA kinases to the Spirochaetota taxonomy tree
87 (Figure S1). Based on the topology of this tree, it appears that the major chemosensory
88 systems in the genomes from the Spirochaetota phylum are: F1 (Leptospirae), a transitional
89 hybrid F1/F2 system (Brachyspirae), and F2 (Spirochaetia) (Fig. S2). Therefore, we
90 conclude that F2 systems are exclusive to the Spirochaetia class, with a few exceptions of
91 lateral gene transfer.
92
93 The main architectural difference of the F2 system compared to others is the presence of an
94 unusual scaffold protein that consists of an N-terminal CheW domain and a C-terminal
95 CheR-like domain, hereafter referred to as CheW-CheR$_{like}$. Typically, CheR is a
96 methyltransferase that, together with the methylesterase CheB, controls the methylation
97 state of the receptors and thus provides an adaptation system[17]. Our analyses indicate that
98 all Spirochaetia genomes in MiST3 contain CheW-CheR$_{like}$. Furthermore, if we limit our
99 analysis to genomes that are fully sequenced (see Supplementary Methods), CheW-CheR$_{like}$
100 is only found in F2 chemosensory systems.
101
102 To investigate sequence patterns in the CheR protein and the CheR-like domain of CheW-
103 CheR$_{like}$, we produced a sequence dataset with 83 CheR-F2 and 88 CheW-CheR$_{like}$ proteins
104 and summarized them in sequence logos (Fig. S3A). Although the key catalytic residues are
105 conserved in the typical CheR protein, two residues that are essential for CheR to methylate
106 chemoreceptors, R79 and Y218 in *Td* CheR, are modified in the CheW-CheR$_{like}$ protein
107 (R79W and Y218F) [17]. Furthermore, the conserved region at the C-terminus of CheR is not
108 conserved in CheW-CheR$_{like}$. Based on these results we speculate that the CheR$_{like}$ domain
109 does not possess methyltransferase activity. Collectively, our analyses suggest that CheR
110 and CheW-CheR$_{like}$ have different biological functions.
111
112 F2 systems contain three proteins with a CheW domain: the classical scaffold CheW, CheW-
113 CheR$_{like}$, and the P5 domain from the histidine kinase CheA. Phylogenetic mapping of

114 CheW-F2 proteins indicate the location of last common ancestor (Fig. S4, see
115 Supplementary methods). To investigate sequence patterns of the three CheW domains, we
116 analyzed non-redundant sequence datasets of CheW, CheW-CheR$_{like}$, and CheA-F2 from all
117 genomes with at least one CheA-F2. The final alignments for each group contain the CheW
118 domain portion of 74 CheW proteins, 59 CheW-CheR$_{like}$ proteins, and 73 CheA proteins. The
119 sequences of each group are summarized in sequence logos and demonstrate the presence
120 of conserved regions at established interaction interfaces, as well as loop insertions near
121 these interfaces that could confer altered specificity of binding (Fig. S3B).
122

123 **The structure of the *Treponema denticola* (*Td*) chemotaxis array in wild-type cells**

124 Cell poles of intact *Td* cells were imaged by cryo-electron tomography (cryo-ET) and used
125 for three-dimensional reconstructions. Top views (cross-sections through the array) and side
126 views (visualizing the long axes of the receptors) of membrane-associated arrays were
127 clearly visible (Fig. 1A, S5A). Sub-volume averaging revealed the conserved receptor trimer-
128 of-dimers in the typical hexagonal arrangement. Remarkably, several novel features of the
129 chemotaxis arrays are apparent (Fig. 1B). Specifically, a density of unknown origin is located
130 in the center of the receptor hexagons and slightly above the plane of the CheA:CheW rings.
131 This density, which will hereafter be referred to as the middle density, extends from two
132 subunits in the rings (Fig. 2A). Additionally, there are small but distinct puncta of density in
133 between some of the trimer-of-dimer modules (Fig. 1B). However, averages of the arrays at
134 the CheA:CheW layer did not reveal discernible CheA density, indicating either a sparse or
135 disordered distribution of CheA or a highly mobile kinase (Fig. 1C). Remarkably, the sub-
136 tomogram averages reveal the axis of the *Td* cells relative to the chemotaxis arrays,
137 demonstrating that the arrays occupy a preferred orientation with respect to the cell axis
138 (Fig. S5B).
139

140 **Arrays in *T. denticola* deletion mutants**

141 The oxygen-binding diiron protein (ODP) functions as an oxygen sensor for chemotaxis in

142 *Td*, however it is uknown if ODP is an integral component of the array[13]. This protein is
143 genetically coupled to an MCP homolog, TDE2496, that lacks both transmembrane and
144 sensing modules. TDE2496 likely integrates into the cytoplasmic regions of the membrane-
145 bound arrays based on the observation that no cytoplasmic arrays were observed in the
146 tomograms. Moreover, the *Td* genome encodes only one CheA homolog, and cytoplasmic
147 receptors often associate with distinct kinases[9,18]. TDE2496 forms trimers-of-dimers *in vitro*
148 and can modulate CheA activity (Fig. S6A,B). To determine if the presence of ODP
149 (TDE2498) and its cognate receptor (TDE2496) impacts array architecture or integrity, we
150 conducted cryo-ET with two *Td* gene knock-out strains, Δ2498 and Δ2498Δ2496[13].
151 Importantly, deletion of ODP does not impact transcription of TDE2496[13]. The sub-volume
152 averages of these strains reveal distinct differences in array densities compared to the wild-
153 type (WT) strain (Fig. 1B,C, Fig. S5A). Namely, the location of CheA at the CheA:CheW
154 layer (Layer 2, Fig 1C) is now clearly visible. Interestingly, CheA arranges in well-ordered
155 linear rows. Placement of CheA necessarily positions the P3 domain in between two of the
156 trimer-of-dimer modules in each hexagon. This position exclusively corresponds to the

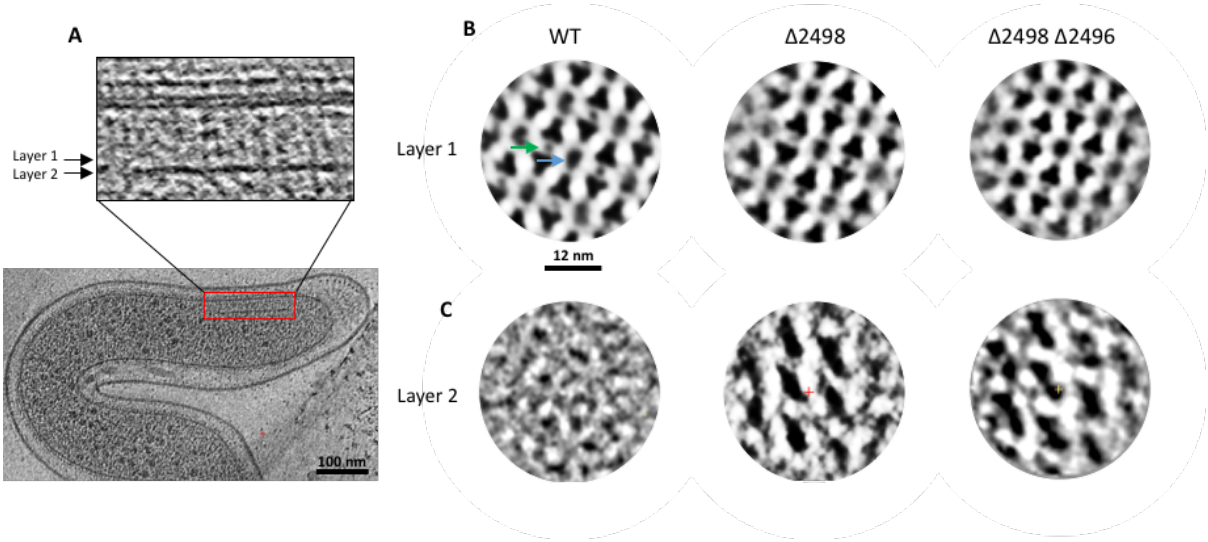

Fig. 1 Cryo-electron tomography of whole *T. denticola* (*Td*) cells reveals the protein arrangement of chemotaxis machinery. (A) Side-views of the membrane-associated chemotaxis apparatus illustrate the location of the receptor layer (Layer 1) and CheA:CheW baseplate (Layer 2). These layers are spaced ~90 Å from one another. (B) Sub-volume averaging of three *Td* strains reveals the universally-conserved receptor trimer-of-dimer arrangement with 12 nm spacing between opposing trimer-of-dimer modules. Notably, density is apparent in the center of the receptor hexagons (blue arrow) and between some receptor trimer-of-dimer modules (green arrow). (C) Sub-volume averages at Layer 2 reveal the organization of CheA. In this arrangement, the density between the trimer-of-dimer modules (green arrow) corresponds to the CheA P3 domain.

157 location of the puncta between receptor trimer-of-dimer modules observed in the WT array,
158 indicating that this density represents the P3 domain (Layer 1, Fig. 1B). Like the WT arrays,
159 the cell axis relative to the chemotaxis arrays is also apparent in these sub-tomogram
160 averages and matches the preferred array orientation in the WT cells (Fig. S5B).
161

162 **Analyses of the CheW-CheR$_{like}$ protein in *T. denticola***

163 To determine the composition of the middle density in the *Td* arrays, we considered the
164 unique chemotaxis proteins in spirochete
165 genomes. As shown above, CheW-CheR$_{like}$ is
166 a conserved component of the F2 Spirochaetia
167 chemotaxis system (Fig. S2). In *Td,* a 28-
168 residue linker in CheW-CheR$_{like}$ separates the
169 two domains and is predicted to be largely
170 helical (JPred), and the gene is co-transcribed
171 with the only CheA, CheX, and CheY proteins
172 in the genome (Fig. S6C,D)[18]. Furthermore,
173 the purified CheW-CheR$_{like}$ protein dimerizes
174 and interacts with CheA, as evidenced by its
175 ability to alter autophosphorylation activity (Fig.
176 2C,D, Fig. S6E,F). Therefore, we postulated
177 that the middle density may be comprised of
178 two dimerized CheR$_{like}$ domains that extend
179 from the CheW units harbored within the
180 CheA:CheW rings.
181

182 A *Td* strain lacking the CheR$_{like}$ domain
183 (ΔCheR$_{like}$) reveals a significant decrease in

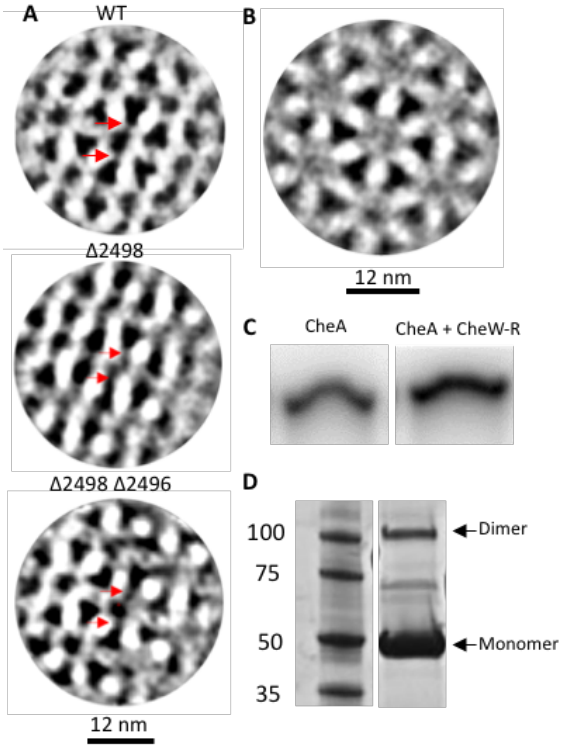

Fig. 2 Investigations into the identity of the density located in the center of the receptor hexagons, referred to as the middle density. (A) In Layer 1, the middle density extends to two positions in the CheA:CheW rings for all three *Td* strains (red arrows). (B) Deletion of a CheR-like domain that is covalently attached to the C-terminus of a CheW domain generates sub-tomogram averages that lack the middle density feature. (C) Radioisotope assays that monitor CheA autophosphorylation with [γ-^{32}P]ATP demonstrate that CheW-CheR$_{like}$ influences CheA activity *in vitro*. Bands are from non-adjacent lanes on the same gel. (D) Purification of CheW-CheR$_{like}$ followed by Native PAGE gel analysis reveals the presence of a protein monomer (49 kDa) and protein dimer (98 kDa). Bands are from non-adjacent lanes on the same gel.

184 the prevalence and size of the arrays (Fig. S5A). Due to the small size of the arrays in
185 ΔCheR$_{like}$, only 194 particles were available for sub-tomogram averaging, but the resulting
186 averages clearly demonstrate that the middle density is no longer present (Fig. 2B, S5A).
187 Like the WT strain, the CheA density below the rings in ΔCheR$_{like}$ is not apparent.
188

189 **Protein interfaces in the CheA:CheW:CheW-CheR$_{like}$ rings**

190 Bioinformatics analyses demonstrate that all functional Spirochaetota F2 chemotaxis
191 systems possess a CheW-CheR$_{like}$ homolog and at least one classical CheW protein. As
192 only two of the CheW subunits in the hexagonal rings extend to the middle density (which
193 probably arises from the CheW-CheR$_{like}$ protein), and two of the ring positions are occupied
194 by CheA P5, it is likely that the other two positions are occupied by the classical CheW
195 protein. (Fig. 2A, S7). Within this arrangement three unique interaction interfaces are
196 possible, interface 1 occurs between CheA P5 and the classical CheW (as seen in canonical
197 systems), interface 2 occurs between CheA P5 and the CheW domain of CheW-CheR$_{like}$,
198 and a third interface (interface 3) occurs between the classical CheW and the CheW domain
199 of CheW-CheR$_{like}$ (Fig. S7). To explore the binding interfaces within the *Td* rings, we
200 analyzed homology models of the classical CheW, the CheW domain of CheW-CheR$_{like}$, and
201 the CheA P5 domain. The CheW models were generated using a crystal structure of
202 *Thermoanaerobacter tengcongensis* (*Tt*) CheW as the template (PDB ID: 2QDL), and the
203 CheA P5 model was generated using a cryo-EM structure of *E. coli* CheA P5 (PDB ID:6S1K)
204 (Fig. S8A-C)[2,19]. Three of the four regions with lowest sequence conservation among the
205 three domains are located at interfaces 1-3 (Fig. S9). Alignment of the *Td* CheW and CheA
206 P5 models to a crystal structure of *Tm* CheW in complex with *Tm* CheA P5 (PDB ID: 3UR1)
207 further illustrates that these regions are located at the CheW:P5 ring interfaces (Fig S9)[20].
208 Mapping the variable regions onto the sequence logos of the F2 CheW domains
209 demonstrates that they evolved different sequence patterns in these regions, with the
210 exception of the variable region that is not located at the interaction interface (region 2, Fig.
211 S9, S3B).

212

213 **CheA arrangement and array curvature in *T. denticola***

214 Sub-tomogram averaging reveals that *Td* CheA forms a linear arrangement across the
215 chemotaxis array, linking the CheA:CheW rings into extended 'strands' that are held
216 together by receptor:CheA/W interactions (Fig. 3A,B). The orientation of the strands are
217 apparent in the sub-tomogram averages and run relatively perpendicular to the axis of the
218 cells (Fig. S10A). The array densities at Layer 1 (receptors, P3, and $CheR_{like}$) produce
219 apparent lines in the cryo-ET reconstructions that, like the sub-tomogram averages, run
220 parallel to the cell axis (Fig. 3C,D)[21]. This arrangement allows interactions that hold the
221 strands together to occur with minimal bending (Fig. 3E,F). Indeed, the angle between the
222 cell axis and these lines in the cells is 10.4 +/- 8.6°, (*n* = 26 cells) and no significant
223 difference was found among the three *Td* strains measured (Table S1A). As the
224 CheA:CheW strands are perpendicular to these lines in the sub-tomogram averages, they
225 will be oriented at an angle of 55.4 +/- 8.6° with respect to the cell axis (Fig. S10A).

226

227 Previous studies in *Ec* and *Vc* demonstrate that the chemotaxis arrays can
228 accommodate vastly different curvatures between lysed and artificially small mini-cell
229 strains[1,3,22]. However, *Td* cells demonstrate a significantly higher curvature of the cell
230 membrane than organisms investigated for their chemotaxis arrangement thus far [1,5,22]. As a
231 measure of comparison, the *Vc* mini-cells used in a previous study have an inner membrane
232 curvature of 9.15 +/- 4.5 /µm (radius 1092 Å, *n* = 6 cells), and the *Td* cells have an inner
233 membrane curvature of 35.8 +/- 6.6 /µm (radius: 279 Å, *n* = 10 cells) (Fig. S10B,C, Table
234 S1B,C). Additionally, the measured curvature of the *Td* CheA:CheW baseplate is 65.6 +/- 19
235 /µm (radius: 152 Å, *n* = 10 cells) (Fig. S10B, Table S1C).

236

237 The CheA:CheW rings present in a crystal structure (PDB ID: 3UR1) are flat and ~95 Å in
238 diameter (Fig. S11A)[20]. The length across two rings connected by a dimeric CheA is 224 Å
239 (Fig. 11B). To determine the extent of bending that would need to occur in the two

240 CheA:CheW rings if they ran perpendicular to the cell axis, the 224 Å rings were modeled as
241 a chord in a circle with radius 152 Å. Using the equation $h = r - \sqrt{r^2 - L^2}$ (where h is the
242 height of the circular segment, r is the circle radius, and L is half the chord length (224 Å /2)),
243 the height of the circular segment is 49.2 Å (Fig. S11B). Therefore, the center of the two
244 rings (the P3 domain) must bend by an average of 49.2 Å toward the cell membrane to
245 accommodate the cell curvature. Using the same equation above (where L is 95 Å /2), the
246 height of the circular segment is 7.6 Å (Fig. S11A). Therefore, in *Td,* the center of a single
247 ring must bend toward the membrane by an average of 7.6 Å to align to the measured
248 baseplate curvature.

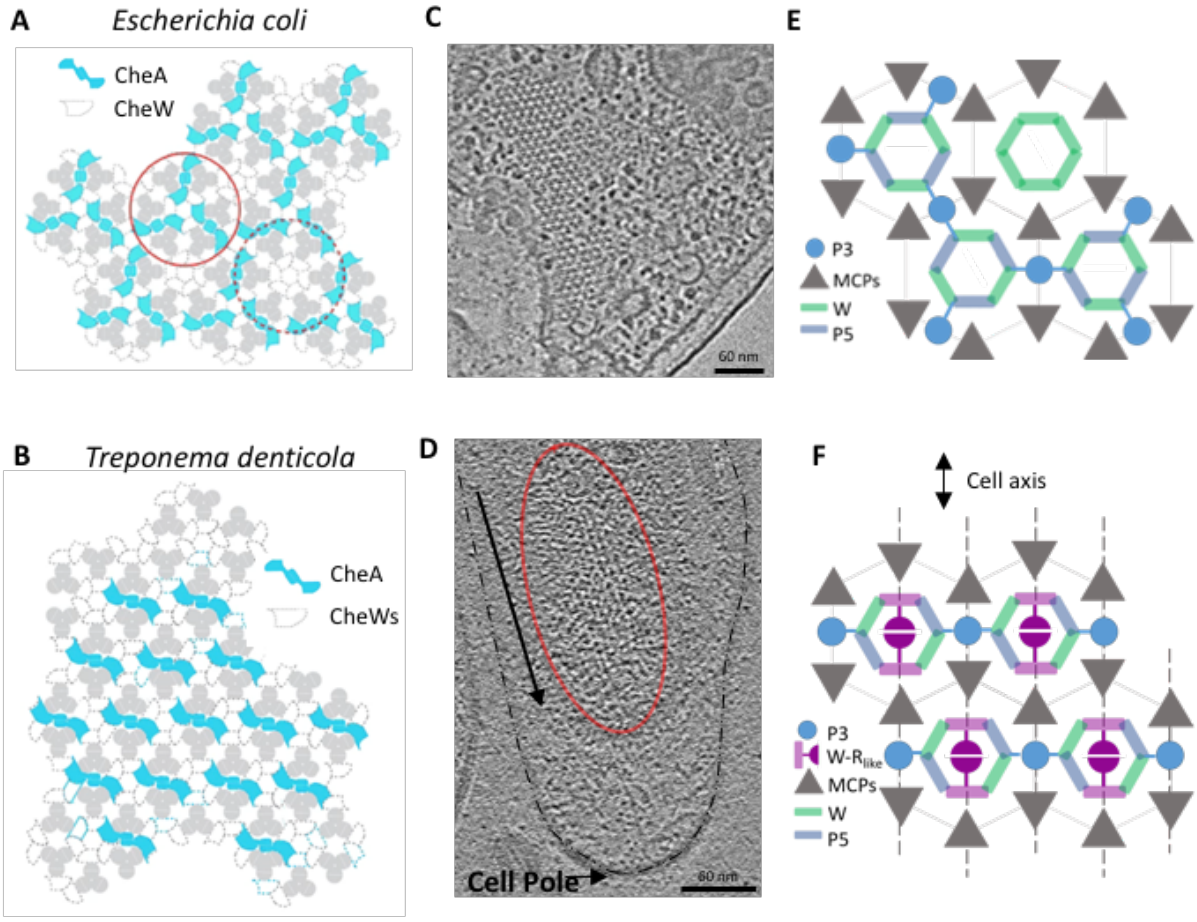

249

Fig. 3 The organization of CheA in *Td* differs from all previously reported arrangements. (A) The hexagonal arrangement of CheA in *E. coli* and other canonical chemotaxis systems. (B) In *Td,* CheA is arranged with a strict linear organization, producing 'strands' of CheA:CheW rings linked by the CheA P3 domain. (C) The receptor densities in *Ec* (Layer 1) are apparent and hexagonal. Figure adapted from Briegel A. et al. 2010.[21] (D) The densities at Layer 1 in *Td* (red oval) produce apparent lines of receptors, P3 and the middle density (CheR-like) that follow the axis of *Td* cells (black arrow). (E) *Ec* arrays possess radial P6 symmetry where all interaction interfaces are equally curved. (F) The *Td* array has a two-fold symmetry arrangement that allows receptor:CheA/W interactions that hold the CheA:CheW strands together to occur with minimal bending. Dashed lines represent the apparent lines in the tomograms.

250 **Spirochetes possess an atypical dimerization domain**

251 The cryo-ET results reveal density corresponding to the P3 domain, which has not been
252 previously reported in *in vivo* arrays. Sequence alignments of *Td* CheA with CheA homologs
253 from a variety of model bacteria with previously characterized chemotaxis systems indicate
254 that in *Td* CheA an additional ~50 residues join the canonical dimerization domain (P3)
255 helices (Figure S12A)[4]. CheA homologs from other spirochete genera including Borrelia and
256 Brachyspira also possess additional residues in this region (Fig. S12B)[23]. Analysis of non-
257 redundant P3 domains from all CheA classes reveal general sequence conservation in the
258 canonical helices but highly divergent sequences at these additional residues (Fig. S13A).
259 Furthermore, CheA-F2 proteins contain the most residues in this non-conserved region (Fig.
260 S13B,C). The x-ray crystal structure of the isolated *Td* P3 domain (PDB ID: 6Y1Y, Fig. 4,
261 Table S2) reveals that the additional residues adopt the coil-coiled motif of the classic
262 dimerization domain with the exception of a break in one of the helices, producing a
263 discontinuous coiled-coil (Fig. 4, S14A). Interestingly, aromatic residues (Phe, Tyr) cluster
264 near the helix breakages and unusual
265 core packing of these residues allows
266 for maintenance of a coiled-coil register
267 despite a disruption of helical heptad
268 repetition in the C-terminal helix (Fig.
269 S14A). The net result is a distortion in
270 the alignment of the hairpin tip, the
271 consequence of which is currently
272 unknown. Differing orientations of Tyr83
273 in the two subunits produces
274 asymmetry in the added tip region
275 (Fig. S14B,C). Fitting the new P3
276 domain into an all-atom chemotaxis

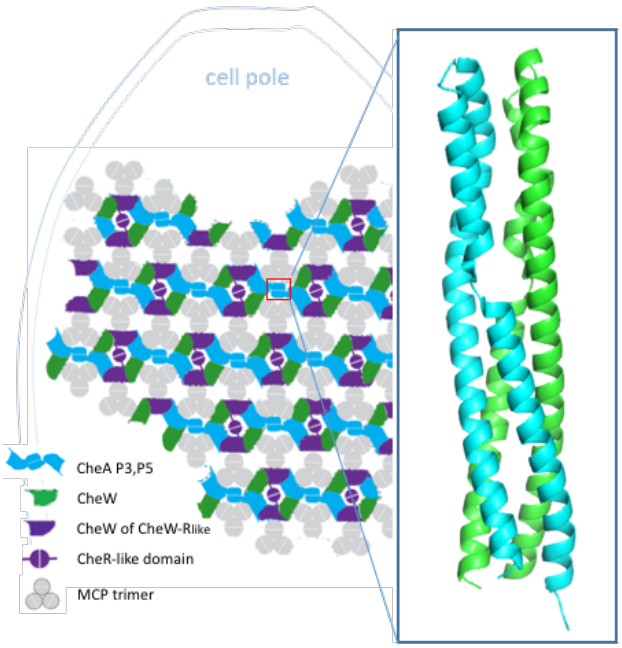

Fig. 4 The arrangement of chemotaxis proteins in *Td.* The linear organization of CheA produces 'strands' of CheA:CheW rings that are perpendicular to the cell axis and are linked by an atypical P3 domain.

array that was generated for previous molecular dynamics simulations (PDB ID: 3JA6) shows that these additional helices are within a ~15 Å from receptors (Fig. S14D)[12]. Additionally, the handedness of the helix connection in the *Td* P3 domain differs from that of *Thermotoga maritima* CheA and rather matches helix connectivity of sensor kinase DHP domains[24,25].

Discussion

Here, we reveal the protein arrangement of F2 chemotaxis arrays through cryo-ET of intact *T. denticola* (*Td*) cells. *Td* cells are thin and cyndrillical, producing a cell that is polarized in shape and membrane curvature; the membrane has extremely high curvature perpendicular to the cell axis and lower curvature parallel to the axis. In accordance with this feature, the *Td* arrays are polarized and assume a preferred orientation with respect to the cell axis. In this system, three proteins comprise the rings at the receptor tips: CheA, CheW, and a CheW-CheR$_{like}$ protein. Like the *Ec* system, these proteins in *Td* are integrated into the array with strict organization[1,22]. However, a linear arrangement of CheA is present that generates 'strands' of rings interlinked by the CheA dimerization domain (P3). The strands run perpendicular to the axis of the *Td* cells, resulting in substantial bending of inter-linked rings. Presumably, the unique binding interfaces in the CheA:CheW rings generate bent interfaces with the appropriate curvature. Furthermore, this directional distinction allows for some array contacts to follow the cell axis and remain undistorted. The deleterious effect on array integrity with the loss of the CheR$_{like}$ domain strongly suggests that CheR$_{like}$ dimerization plays a key role in array assembly and stabilization. The strict linear arrangement of CheA could be facilitated by the composition of the *Td* rings; three unique protein interfaces are present in the rings and restrict CheA P5 integration (i.e. CheA P5 can only occupy these two positions in the six-member ring). Furthermore, the *Td* CheA P3 domain is clearly discernible in the averaged tomograms, which has not been previously observed *in vivo*[5,9,22]. As the CheA:CheW rings have to undergo substantial bending to accommodate the baseplate curvature, the elongated P3 domain may have evolved to stabilize CheA

305 dimerization by increasing the interface area and furthermore may encourage interactions
306 with neighboring receptors[12]. Due to the curvature, the receptor trimer-of-dimer modules are
307 expected to be further splayed, and the elongated P3 may compensate for the increased
308 distance between receptors and P3. As *Td* cells have the smallest average diameter (0.1 –
309 0.4 μm) of all bacteria with determined chemotaxis architectures thus far, and the novel
310 linear arrangement of CheA produces arrays that can better accommodate its unique
311 membrane curvature, we surmise that the array architecture in *Td* is an adaptation that
312 evolved to produce an extended chemoreceptor apparatus in a highly curved and
313 asymmetric membrane[4,5,9]. Importantly, bioinformatics analyses indicate that the unique
314 protein features seen in *Td* are exclusive to Spirochaetia F2 systems.
315
316 Unexpectedly, the placement of CheA in WT *Td* arrays could not be discerned (with the
317 exception of the P3 domain), but was clearly visible in two *Td* mutants (Δ2498,
318 Δ2498Δ2496). As the density corresponding to the P3 domain in the WT strain is clearly
319 discernible, the sparse density corresponding to all other CheA domains (P1, P2, P4, P5) is
320 not attributed to low CheA incorporation in these arrays. These results indicate that the
321 kinase is highly mobile or more disordered in the WT strain, but is more constrained when
322 ODP (TDE2498) is deleted, suggesting that ODP directly affects array structure. However,
323 densities in the three strains do not designate an obvious position for ODP, indicating that
324 ODP may not be an integral component of the array, but rather peripherally interacts with the
325 chemotaxis machinery or influences its architecture through other means, perhaps related to
326 its signaling properties.
327
328 In summary, we illustrate a novel chemotaxis arrangement that has evolved to compliment
329 the spirochetes' high membrane curvature and asymmetry. Therefore, it is likely that the
330 behavior and characteristics of chemoreceptor arrays in general can be influenced by
331 perturbing the shape of the cell membrane. Recent studies with *Ec* ultra-minicells (the
332 smallest mini-cells available to date) produce densities corresponding to portions of

333 chemoreceptors that have not been observed before[3]. However, it is possible that increased
334 membrane curvature limits movement of the transmembrane receptors, resulting in
335 increased receptor localization and resolution. Furthermore, the use of lipid-templating has
336 been extensively used to assemble arrays *in vitro* for cryo-ET and reconstitutes the
337 chemotaxis apparatus in a perfectly flat formation[2,12]. While cryo-ET experiments of *in vivo*
338 *Ec* arrays consistently shows the CheA P3 density to be too sparse to determine its position,
339 cryo-ET of *in vitro* lipid-templated *Ec* arrays clearly defines the P3 position. If the P3 domain
340 does engage receptors, this discrepancy may suggest that lipid-templating abrogates this
341 native behavior. Furthermore, it is unclear how the *Td* chemotaxis arrangements affects
342 cooperative behavior in the arrays as linear CheA:CheW strands are only connected through
343 receptor interactions. Investigations into this system may reveal alternative mechanisms for
344 cooperative behavior than what have been reported. Collectively, our results illustrate the
345 importance of investigating transmembrane systems *in situ*, and that examining systems in
346 non-model organisms can lead to new, unexpected advances for understanding the
347 remarkable signaling system of bacterial chemotaxis.
348

349 **Acknowledgements**

350 This work is part of the research programme National Roadmap for Large-Scale Research
351 Infrastructure 2017 – 2018 with project number 184.034.014, which is financed in part by the
352 Dutch Research Council (NWO). This work was funded by a grant from the National
353 Institutes of Health: R35GM122535 awarded to BRC, R01AI078958 and R01DE023080 to
354 CLI, and by the European Union under a Marie-Sklodowska-Curie COFUND LEaDing
355 fellowship to ARM. We thank the Netherlands Centre for Electron Nanoscopy (NeCEN) for
356 access to cryo-ET data collection facilities, and NE-CAT at the Advanced Photon Source for
357 access to X-ray crystallography data collection facilities. NE-CAT is supported by
358 NIH/NIGMS awards P30 GM124165 and S10 RR029205.
359
360

361 **Author contributions.** A.R.M., D.R.O, K.K., C.L., B.R.C, and A.B. designed research; A.R.M.,
362 D.R.O., and K.K. performed research; A.R.M., D.R.O, W.Y., K.K., and A.S. analyzed data; and
363 A.R.M., D.R.O, and A.B. wrote the paper with input from all authors.
364
365 **Competing interest.** The authors declare no competing interests.
366
367 **Materials and Correspondence.** Correspondence and materials requests should be addressed to A.
368 Briegel at a.briegel@biology.leidenuniv.nl.
369
370

371 1. Yang, W., Alvarado, A., Glatter, T., Ringgaard, S. & Briegel, A. Baseplate variability of
372 *Vibrio cholerae* chemoreceptor arrays. *Proc. Natl. Acad. Sci.* **115**, 201811931 (2018).
373 2. Cassidy, C. K. *et al.* Structure and dynamics of the E. coli chemotaxis core signaling
374 complex by cryo-electron tomography and molecular simulations. *Commun. Biol.* **3**,
375 1–10 (2020).
376 3. Burt, A. *et al.* Complete structure of the core signalling unit of the E. coli
377 chemosensory array in an optimised minicell strain. *Nat. Commun.* 1–9 (2019).
378 doi:10.1038/s41467-020-14350-9
379 4. Briegel, A. *et al.* Universal architecture of bacterial chemoreceptor arrays. *Proc. Natl.*
380 *Acad. Sci. U. S. A.* **106**, 17181–17186 (2009).
381 5. Briegel, A. *et al.* Bacterial chemoreceptor arrays are hexagonally packed trimers of
382 receptor dimers networked by rings of kinase and coupling proteins. *Proc. Natl. Acad.*
383 *Sci.* **109**, 3766–3771 (2012).
384 6. Hazelbauer, G. L., Falke, J. J. & Parkinson, J. S. Bacterial chemoreceptors: high-
385 performance signaling in networked arrays. *Trends Biochem. Sci.* **33**, 9–19 (2008).
386 7. Pedetta, A., Parkinson, J. S. & Studdert, C. A. Signalling-Dependent Interactions
387 Between the Kinase-Coupling Protein CheW and Chemoreceptors in Living Cells. **93**,
388 1144–1155 (2015).

389 8. Muok, A. R., Briegel, A. & Crane, B. R. Regulation of the chemotaxis histidine kinase
390 CheA: A structural perspective. *Biochim. Biophys. Acta - Biomembr.* **1862**, 183030
391 (2019).
392 9. Briegel, A. *et al.* Structure of bacterial cytoplasmic chemoreceptor arrays and
393 implications for chemotactic signaling. *Elife* **2014**, 1–16 (2014).
394 10. Bhatnagar, J. *et al.* Structure of the ternary complex formed by a chemotaxis receptor
395 signaling domain, the CheA histidine kinase, and the coupling protein CheW as
396 determined by pulsed dipolar ESR spectroscopy. *Biochemistry* **49**, 3824–41 (2010).
397 11. Zhang, K. *et al.* Two CheW coupling proteins are essential in a chemosensory
398 pathway of Borrelia burgdorferi. *Mol. Microbiol.* **85**, 782–794 (2012).
399 12. Cassidy, C. K. *et al.* CryoEM and computer simulations reveal a novel kinase
400 conformational switch in bacterial chemotaxis signaling. *Elife* **4**, 1–20 (2015).
401 13. Muok, A. R. *et al.* A di-iron protein recruited as an Fe[II] and oxygen sensor for
402 bacterial chemotaxis functions by stabilizing an iron-peroxy species. *Proc. Natl. Acad.*
403 *Sci.* **116**, 14955–14960 (2019).
404 14. Wuichet, K. & Zhulin, I. Origins and Diversification of a Complex Signal Transduction
405 System in Prokaryotes. *Sci Signal* **128**, 1–27 (2010).
406 15. Gumerov, V. M., Ortega, D. R., Adebali, O., Ulrich, L. E. & Zhulin, I. B. MiST 3.0: an
407 updated microbial signal transduction database with an emphasis on chemosensory
408 systems. *Nucleic Acids Res.* **48**, D459–D464 (2020).
409 16. Parks, D. H. *et al.* A standardized bacterial taxonomy based on genome phylogeny
410 substantially revises the tree of life. *Nat. Biotechnol.* **36**, 996 (2018).
411 17. García-Fontana, C. *et al.* High specificity in CheR methyltransferase function: CheR2
412 of pseudomonas putida is essential for chemotaxis, whereas CheR1 is involved in
413 biofilm formation. *J. Biol. Chem.* **288**, 18987–18999 (2013).
414 18. Greene, S. R. & Stamm, L. V. Molecular characterization of a chemotaxis operon in
415 the oral spirochete, Treponema denticola. *Gene* **232**, 59–68 (1999).
416 19. Yao, W., Shi, L. & Liang, D. C. Crystal structure of scaffolding protein CheW from

417 thermoanaerobacter tengcongensis. *Biochem. Biophys. Res. Commun.* **361**, 1027–
418 1032 (2007).
419 20. Li, X. *et al.* The 3.2 Å resolution structure of a receptor:CheA:CheW signaling complex
420 defines overlapping binding sites and key residue interactions within bacterial
421 chemosensory arrays. *Biochemistry* **52**, 3852–3865 (2013).
422 21. Briegel, A. *et al.* The mobility of two kinase domains in the Escherichia coli
423 chemoreceptor array varies with signaling state . **14**, 384–399 (2010).
424 22. Yang, W. *et al.* In situ conformational changes of the escherichia coli serine
425 chemoreceptor in different signaling states. *MBio* **10**, 1–14 (2019).
426 23. Sze, C. W., Zhang, K., Kariu, T., Pal, U. & Li, C. Borrelia burgdorferi needs
427 chemotaxis to establish infection in mammals and to accomplish its enzootic cycle.
428 *Infect. Immun.* **80**, 2485–2492 (2012).
429 24. Greenswag, A., Muok, A., Li, X. & Crane, B. Conformational Transitions that Enable
430 Histidine Kinase Autophosphorylation and Receptor Array Integration. *J. Mol. Biol.*
431 **427**, 87–92 (2016).
432 25. Bilwes, A. M., Alex, L. A., Crane, B. R. & Simon, M. I. Structure of CheA, a signal-
433 transducing histidine kinase. *Cell* **96**, 131–141 (1999).
434
435

436 **Supplementary Methods and Materials**

437 **Data availability**

438 The cryo-ET sub-tomogram averages that support these findings are deposited in the Electron
439 Microscopy Data Bank (EMDB) with accession codes EMD-10784, EMD-10785, EMD-10786, EMD-
440 10787, EMD-10788, EMD-10790. The protein x-ray crystallography structure that supports these
441 findings is deposited in the Protein Data Bank (PDB) with accession code 6Y1Y. These depositions
442 will be publicly available with publication.

443

444 **Code availability**

445 All custom-made scripts are available to editors and referees upon request. These scripts will be
446 publicly available with publication.

447

448 **Bacterial strains, culture conditions, and oligonucleotide primers**

449 *Treponema denticola* (*Td*) ATCC 35405 (wild-type) was used in this study. The *Td* deletion
450 mutants, Δ2498 and Δ2498Δ2986, were generated in a previous study[2]. Cells were grown in
451 tryptone-yeast extract-gelatin-volatile fatty acids-serum (TYGVS) medium at 37°C in an
452 anaerobic chamber in presence of 85% nitrogen, 10% carbon dioxide, and 5% hydrogen[1].
453 *Td* mutants were grown with an appropriate antibiotic for selective pressure as needed:
454 erythromycin (50 µg/ml) and gentamycin (20 µg/ml). *Escherichia coli* 5α strain (New England
455 Biolabs, Ipswich, MA) was used for DNA cloning. The *E. coli* strains were cultivated in
456 lysogeny broth (LB) supplemented with appropriate concentrations of antibiotics. The
457 oligonucleotide primers for PCR amplifications used in this study are listed in Table S3.
458 These primers were synthesized by IDT (Integrated DNA Technologies, Coralville, IA).

459

460 **Construction of a CheR truncated mutant (ΔCheR$_{like}$)**

461 *TDE1492::ermB* (Fig. S15) was constructed to replace the CheR-like domain (8781-1,308 nt) in
462 *TDE1492 with* a previously documented erythromycin B resistant cassette (*ermB*)[3]. The
463 *TDE1492::ermB* vector was constructed by two-step PCR and DNA cloning. To construct this vector,
464 the 5` end of *TDE1492* region and the downstream flanking region were PCR amplified with primers

465 P_1/P_2 and P_3/P_4, respectively, and then fused together with primers P_1/P_4, generating Fragment 1. The
466 Fragment 1 was cloned into the pMD19 T-vector (Takara Bio USA, Inc, Mountain View, CA). The
467 *ermB* cassette was PCR amplified with primers P_5/P_6, generating Fragment 2. The Fragment 2 was
468 cloned into the pGEM-T easy vector (Promega, Madison, WI). The Fragment 1 and 2 were digested
469 using *Not*I and ligated, generating the *TDE1492::ermB* plasmid. The primers used here are listed in
470 Table S3. To delete *TDE1492*, the plasmid of *TDE1492::ermB* was transformed into *Td* wild-type
471 competent cells via heat shock, as previously described[4]. Erythromycin-resistance colonies that
472 appeared on the plates were screened by PCR for the presence of *ermB* and absence of *TDE1492*
473 *(781-1,308 nt)* gene**.** The PCR results showed that the *TDE1492 (781-1,308 nt)* gene was replaced by
474 *ermB* cassette as expected (Fig. S15). One positive clone (*ΔTDE1492*) was selected for further study.
475

476 **Bioinformatics software and resources**

477 The datasets used in the bioinformatics analysis were built using data from Microbial Signal
478 Transduction Database v3 (MiST3) accessed February 2020[5] and the Genome Taxonomy Database
479 v89 (GTDB) [6]. We built custom scripts using TypeScript-3.7.5 and NodeJS-12.13. To make these
480 scripts, we also used packages publicly available at the node package manager repository (npm): we
481 used RegArch-1.0.1[7] to separate CheW-$CheR_{like}$ from other CheWs, gtdb-local-0.0.12
482 (https://npmjs.com/package/gtdb-local) to use the GTDB taxonomy, Phylogician-TS-0.10.1-4
483 (https://npmjs.com/package/phylogician-ts) to visualize and manipulate the phylogenetic trees,
484 BioSeq-TS-0.2.4 (https://npmjs.com/package/bioseq-ts) to handle protein sequences and MiST3-TS-
485 0.7.6 (https://npmjs.com/package/mist3-ts) to access MiST3 API. Multiple sequence alignments were
486 produced using L-INS-I algorithm from the MAFFT package. To reduce redundancy in sequence
487 datasets we used CD-HIT v4.6[8] with unaligned sequences and Jalview[9] with aligned sequences.
488 RAxML v8.2.10[10] was used to perform phylogenetic reconstructions, and low support branches in the
489 phylogenetic trees were collapsed with TreeCollapseCL4[11]. Sequence logos were built using Weblogo
490 3.7[12].
491

492 **Bioinformatics scripts and pipelines**

493 We collected all information on the proteins classified as CheA (96,434) and CheW (134,165). To
494 process this dataset we built several scripts and pipelines to produce the tables, figures and datasets
495 used in this analysis (Fig. S16). The scripts are found in Supplementary File 1.
496
497 **Chemosensory profile of Spirochaetotas**
498 The "spiro-pipeline" selects all genomes from Spirochaetota phylum using gtdb-local package to
499 access GTDB v89, then it filters only the genomes that are also present in MiST3 database. It collects
500 the information on MiST for each genome and appends the complete taxonomy information from
501 GTDB and signal transduction profiles. Finally, the pipeline builds the table with the information in
502 markdown (Dataset 2).
503
504 **Chemosensory profile of genomes with at least one CheA-F2**
505 The "chea-pipeline" starts from the raw dataset taken from MiST3 database with information on
506 96,434 CheA genes. Based on MiST3 classification it selects the genomes with at least one CheA-F2
507 sequences and fetches information about these genomes. At this step, it also checks with the list
508 generated by the "wr-pipeline" of the genomes containing CheW-CheR$_{like}$. It proceeds to append
509 chemosensory information for each genome and GTDB taxonomy. At this step the pipeline splits into
510 four pathways, where one parses the information to build the Dataset 1 and the other three build
511 FASTA formatted files with sequences from: CheA-F2, CheR-F2, CheW-CheR$_{like}$ and all CheWs
512 belonging to genomes with at least 1 CheA-F2. We noticed that MiST3 currently misclassifies some
513 CheR proteins, so we used RegArch to filter out false positives. We also used RegArch to separate
514 CheW and CheW-CheR$_{like}$ sequences as MiST3 classifies both as CheW (scaffold). The RegArch
515 definitions can be found in the script 'regArchDefinitions.ts' of the source code in Supplementary File
516 1.
517
518 In MiST3[12], 306 genomes contain at least 1 CheA-F2 (Dataset 1) with three exceptions: two of them
519 belong to Acidobacteriota phylum,and one from Planctomycetota, which suggest that the presence of
520 an F2 system in these genomes (outside of the Spirochaetota phylum) is the consequence of lateral
521 gene transfer. Of the 306 genomes with at least one CheA-F2, only the following lack the CheW-
522 CheR$_{like}$ protein: the three non-Spirochaetota genomes mentioned previously, 40 genomes of the

523 Brachyspirae class, and three genomes from the order Borreliales (Fig. S2). Interestingly, the
524 Borreliales genomes do appear to have the CheW-CheR$_{like}$ gene, except there is no gene product
525 associated with them in the MiST3 database.
526
527 **Classification of CheW**
528 CheW proteins are not classified in MiST3. In order to make comparisons between the sequences of
529 CheW domains in F2 systems, we must first select only CheW-F2. We first assign to the F2 class all
530 the canonical CheW found in genomes with a single CheA-F2. Contrary to the F2 systems where the
531 canonical CheW is not present in the chemosensory gene clusters, other classes do contain their
532 canonical CheW within the rest of the gene cluster. CheW found within 5 genes from a classified
533 CheA were assigned to the same class as CheA. To perform this classification, we selected the 598
534 full-length CheW sequences generated by the chea-pipeline. We used CD-HIT to remove 405
535 redundant sequences (-c 1). Next, we ran the "classify-w" pipeline on the remaining sequences (193).
536 The pipeline reads the identifiers of the sequences and fetches the chemotaxis profile from MiST3 for
537 each genome. It classifies CheWs as F2 classes if there is only 1 CheA of the class F2 in the profile.
538 Next, it fetches the gene neighborhood (5 genes up and downstream) of the remaining CheWs and
539 assigns a matching class if there is a classified CheA within these genes. We also aligned the
540 sequences (193) with the L-INS-I algorithm of the MAFFT package, produced a phylogeny with 1000
541 rapid bootstrap using RAxML (-f a -m PROTGAMMAIAUTO -N 1000) and collapsed the phylogeny
542 using TreeCollapse4 at 50% bootstrap. We mapped the CheW classification to the CheW tree in
543 Figure S2. We expanded the F2 classification to the 74 sequences within the branch with only CheW-
544 F2 sequences.
545
546 **Comparison of the CheW domains in CheA, CheW-CheR$_{like}$ and CheW**
547 We put together the sequences from CheA-F2 and CheW-CheR$_{like}$ (both trimmed by the PFAM model
548 for the CheW domain, already annotated in MiST3) and the full sequence of the CheW-F2 selected in
549 the previous step. We then use L-INS-I algorithm to align the sequences and Jalview to manually
550 inspect and eliminate identical redundant sequences. Finally, we trimmed the whole alignment based
551 on the boundaries of CheA-F2 and CheW-CheR$_{like}$ and eliminated one incomplete sequence:
552 GCF_000413015.1-HMPREF1221_RS07250. The final alignment had a total of 206 sequences: 73

553 CheA, 59 CheW-CheR$_{like}$ and 74 CheW. We separated the alignments into individual files and built
554 sequence logos to summarize the amino-acid diversity in each position for each group (Fig. S3B).
555
556 **Comparison of CheR domains**
557 First, we added together the trimmed part matching the CheR domain of the CheW-CheR$_{like}$
558 sequences and the 292 sequences of the CheR protein. We then aligned the 550 sequences using L-
559 INS-I. We used Jalview to inspect the alignment and remove identical redundant sequences. The final
560 alignment had the CheR domain of 83 CheR and 83 CheW-CheR$_{like}$ proteins. We separated the
561 alignments into individual files and generated independent sequence logos (Fig. S3A).
562
563 **Analyses of CheA P3 domains**
564 The "p3-pipeline" pipeline processes the data for the analysis of the length of P3 domains of all CheA
565 homologs in the MiST3 database. It reads the information for all 96,434 CheAs in the MiST3
566 database, trims the sequence matching the Pfam mode H-kinase_dim and builds FASTA formatted
567 datasets for each chemotaxis class. For each dataset, we used CD-HIT with 75% identity cutoff and
568 aligned them using the L-INS-I algorithm from MAFFT. Using Jalview we manually inspect and edited
569 the alignment to remove divergent sequences that opens major gaps in the alignment. We removed 6
570 F1 sequences, 37 F7 sequences, 20 F8 sequences and 5 F9 sequences. Then we merged the
571 alignment using mafft-profile with each dataset as a seed alignment in a single shot (Fig. S13A). We
572 selected the non-conserved central region of the alignment and measured the number of amino-acids
573 in each sequence (Fig. S13B).
574
575 **Cryo-ET and sub-tomogram averaging of *T. denticola* chemotaxis arrays**
576 Cells were concentrated by centrifugation, and a 1/10 dilution of protein A- treated 10-nm colloidal
577 gold solution (Cell Microscopy Core, Utrecht University, Utrecht, The Netherlands) was added to the
578 cells and mixed by pipeting. 3 µL aliquots of the cell suspension were applied to glow-discharged
579 R2/2 200 mesh copper Quanti-foil grids (Quantifoil Micro Tools, GmbH), the sample was pre-blotted
580 for 30 seconds, and then blotted for 2 seconds. Grids were pre-blotted and blotted at 20 °C and at
581 95% humidity. The grids were plunge-frozen in liquid ethane using an automated Leica EM GP
582 system (Leica Microsystems).

583 Data collection was achieved on a Titan Krios transmission electron microscope (Thermo Fisher
584 Scientific) operating at 300 kV. Images for three strains (WT, Δ2498, Δ2498Δ2986) were recorded
585 with a Gatan K2 Summit direct electron detector with a GIF Quantum energy filter (Gatan) operating
586 with a slit width of 20 eV. Images were taken at a magnification of 42,000×, which corresponds to a
587 pixel size of 3.513 Å. Tilt series were collected using SerialEM with a modified bidirectional tilt scheme
588 (-20° to 60°, followed by -22° to -60°) with a 2° increment. Images for the $\Delta CheR_{like}$ strain were
589 recorded with a Gatan K3 Summit direct electron detector equipped with a GIF Quantum energy filter
590 (Gatan) operating with a slit width of 20 eV. Images were taken at a magnification of 26,000X, which
591 corresponds to a pixel size of 3.27 Å. Tilt series were collected using SerialEM with a bidirectional
592 dose-symmetric tilt scheme (-60° to 60°, starting from 0°) with a 2° increment. For all strains, the
593 defocus was set to − 6μm and the cumulative exposure per cell was 100 e-/A^2.
594 Bead tracking-based tilt series alignment and drift correcting were done using IMOD[13]. CTFplotter
595 was used for contrast transfer function determination and correction[14]. Tomograms were
596 reconstructed using simultaneous iterative reconstruction with iteration number set to 6. Dynamo was
597 used for manual particle picking and sub-tomogram averaging[15,16].
598
599 **Purification of CheA, CheA P3, CheW-$CheR_{like}$, and TDE2496 proteins of *T. denticola***
600 DNA segments encoding the CheA P3 domain, CheW-$CheR_{like}$ protein, and TDE2496 in *T. denticola*
601 were PCR amplified from *Td* genomic DNA using a forward oligonucleotide encoding an NdeI
602 restriction site and a reverse primer encoding an EcoRI restriction site. The CheA protein was
603 amplified using a forward oligonucleotide encoding an NdeI restriction site and a reverse primer
604 encoding an BamHI restriction site. The PCR products were treated with the appropriate restriction
605 enzymes, purified, and ligated into a pet28a plasmid with a poly-Histidine tag and kanamycin
606 resistance marker. The plasmids were transformed into *Escherichia coli* BL21-DE3 cells and 4-8 L of
607 cell culture were grown at 37°C until an O.D. of 0.6 was reached. The flasks were cooled to 21°C and
608 1 mM of IPTG was added to the culture. The cells were harvested after 16 hours of growth. The cells
609 were lysed via sonication in lysis buffer (50 mM Tris pH 7.5, 150 mM NaCl, 5 mM Imidazole) while
610 cooled on ice. The lysate was centrifuged at 20,000 X G for 1 hour at 4°C. The lysate was then run
611 over a gravity-flow purification column containing 3 ml of Nickel-NTA resin. The resin was washed
612 with 10 ml wash buffer (50 mM Tris pH 7.5, 150 mM NaCl, 20 mM Imidazole) and the protein was

613 eluted with 10 ml elution buffer (50 mM Tris pH 7.5, 150 mM NaCl, 200 mM Imidazole) and collected
614 in 1 ml fractions. The fractions were assessed for protein concentration via Bradford reagent and the
615 fractions containing protein were run on a size-exclusion s75 and s200 column systems that
616 monitored absorbance at 280 nm and collected 6 ml fractions. Fractions that contain CheA were
617 concentrated to ~20 mg/ml via centrifugation in a protein concentrator containing a regenerated
618 cellulose filter with a 50 kDa molecular-weight cut-off (MWCO). Fractions that contain CheA P3,
619 CheW-CheR$_{like}$ and TDE2496 were concentrated with a 10 kDa MWCO filter to 32 mg/ml, 11 mg/ml
620 and 7 mg/ml, respectively. The protein solutions were aliquoted, flash frozen in liquid nitrogen, and
621 stored at -80°C. For CheW-CheR$_{like}$, CheA, and CheA P3 domain, the purifications were prepared at
622 ambient temperatures. For TDE2496, the purification was prepared at 4°C.
623
624 **Radioisotope assays**
625 23 µl samples containing 2 µM CheA alone, or 2 µM CheA and 2 µM CheW-CheR$_{like}$, or 2 µM CheA
626 and 2 µM CheW-CheR$_{like}$ with TDE2496 (2 µM or 12 µM), were incubated in 50 mM MOPS pH 7.5,
627 150 mM KCl, 10 mM $MgCl_2$ for 30 minutes at ambient temperatures. Phosphorylation of CheA was
628 initiated by the addition of 2 µl of a solution containing 1 mM ATP mixed and 2-10 µl radiolabeled γ-
629 P^{32} ATP (3000 Ci/mmol, 10 µCi/µL; Perkin Elmer) and quenched with 25 µl of 3X LDS buffer
630 containing 100 mM EDTA pH 8.0 after 1-12 minutes. The samples were run on a native Tris-glycine
631 gel for 2 hours at 120 volts. The gels were dried, placed in a radiocassette for 24 hours, and then
632 imaged with a Typhoon phosphor-imager (GE Healthcare). The intensity of the radio-labeled protein
633 bands were quantified using ImageJ.
634
635 **Quantification of cell curvature**
636 The cell curvature of *Td* whole cells and *V. cholera* minicells was quantified by analyzing images of
637 cross-sections of the cells where top views of chemotaxis arrays are present. For *Td* cells, the inner
638 membrane curvature and CheA:CheW base-plate curvature was quantified. For *Vc* minicells, the
639 inner membrane curvature was quantified. These images were pre-processed with Fiji by placing
640 points along the desired area with a distance of 10 nm between each point. The curvature of the inner
641 membrane was measured with a pre-built plugin for python, called Sabl_mpl, written by Jewett, A.
642 from the Jensen lab (Pasadena, CA)[23]. The “measure 3-point curvature” function was used to select

643 three adjacent points along the inner membrane of the cell and calculate the radius of these points.
644 The radius of the three selected points allowed for the calculation of the local curvature by dividing 1
645 with the measured radius (1/R = c). This was repeated for all points with a “sliding window” approach,
646 where the second point of the initial three points would become the first point, until the desired area
647 was covered.
648
649 **Quantification of array alignment to the cell axis**
650 The angle between the strands of CheA:CheW rings and the *Td* cell axis was quantified using Image
651 J software. 2D images from reconstructions that clearly locate the orientation of the strands and cell
652 axis were chosen for analysis. First, a straight line was drawn from the cell pole down the axis of the
653 cells. Then, a second line was drawn through one of the strands in the array and the angle between
654 the two intersecting lines was quantified. In some cases, the angle was too small (<3°) to be
655 accurately determine so the angle was annotated as 0°.
656
657 **Residue conservation and molecular modeling of *Td* CheW, CheA P5, and the CheW domain of**
658 **CheW-CheR$_{like}$**
659 The protein sequences of the two *Td* CheW domains and *Td* P5 were aligned (Clustal Omega),
660 conservation was calculated based on the alignment (JalView[9]), and the highest variable regions
661 were selected based on conservation (10+ adjacent residues with conservation scores lower than 8).
662 Homology models of *Td* CheA P5, CheW and the CheW domain of CheW-CheR$_{like}$ were generated
663 via the Swiss-Model server using complete residue sequences of each protein as a target[24]. The
664 CheW protein from *Thermoanaerobacter tengcongensis* (*Tt*) (PDB ID: 2QDL) had the highest percent
665 identity to the CheW proteins (37% and 31%) and was therefore used as the structural template. The
666 resulting homology models for *Td* CheW and the CheW domain of CheW-CheR$_{like}$ had a QMEAN of -
667 1.3 and -1.2, respectively. The P5 structure from *Escherichia coli* produced the best homology model
668 for *Td* CheA P5, with QMEAN -0.98 (PDB ID: 6S1K). The homology models were then aligned to the
669 CheW protein and P5 domain in a crystal structure containing *Thermotoga maritima* CheW and CheA
670 P4P5 in complex using PyMol (PDB ID: 3UR1).
671
672 **Crystallization and structural determination of the P3 domain of *T. denticola* CheA**

673 The isolated P3 domain was concentrated to 32 mg/ml and crystallized via hanging drop in 0.1 M
674 Imidazole pH 7.0, 25% PEG 400 using a 1:1 ratio of protein solution to crystallization solution with a
675 final volume of 3 µl. Crystals were apparent within eight hours but increased in size over three days.
676 Crystals were manually picked up in loops, flash cooled and shipped in liquid nitrogen to a beamline
677 (APS, line NE-CAT 24-ID-C, Dectris Pilatus 6M-F Pixel Array detector). The crystals diffracted to ~1.3
678 Å with a C2 symmetry and data was cut-off at 1.5 Å. The diffraction data was scaled and integrated
679 using XDS[17], and phased by molecular replacement with Phaser MR using *ab initio* search models
680 generated through the QUARK server and then ran through the AMPLE pipeline on the CCP4 web
681 server[18–20]. Model improvement was done by several rounds of manual model improvement in COOT
682 followed by automated refinement using Phenix Refine software[21,22].
683

684 1. Ohta, K., Makinen, K. K. & Loesche, W. J. Purification and characterization of an enzyme
685 produced by Treponema denticola capable of hydrolyzing synthetic trypsin substrates. *Infect.*
686 *Immun.* **53**, 213–20 (1986).
687 2. Muok, A. R. *et al.* A di-iron protein recruited as an Fe[II] and oxygen sensor for bacterial
688 chemotaxis functions by stabilizing an iron-peroxy species. *Proc. Natl. Acad. Sci.* **116**, 14955–
689 14960 (2019).
690 3. Goetting-Minesky, M. P. & Fenno, J. C. A simplified erythromycin resistance cassette for
691 Treponema denticola mutagenesis. *J. Microbiol. Methods* **83**, 66–68 (2010).
692 4. Kurniyati, K. & Li, C. pyrF as a counterselectable marker for unmarked genetic manipulations
693 in Treponema denticola. *Appl. Environ. Microbiol.* **82**, 1346–1352 (2016).
694 5. Gumerov, V. M., Ortega, D. R., Adebali, O., Ulrich, L. E. & Zhulin, I. B. MiST 3.0: an updated
695 microbial signal transduction database with an emphasis on chemosensory systems. *Nucleic*
696 *Acids Res.* **48**, D459–D464 (2020).
697 6. Parks, D. H. *et al.* A standardized bacterial taxonomy based on genome phylogeny
698 substantially revises the tree of life. *Nat. Biotechnol.* **36**, 996 (2018).
699 7. Ortega, D. R. & Jensen, G. J. Regular Architecture (RegArch): A standard expression
700 language for describing protein architectures. *bioRxiv* 679910 (2019). doi:10.1101/679910
701 8. Li, W., Jaroszewski, L. & Godzik, A. Clustering of highly homologous sequences to reduce the
702 size of large protein databases. *Bioinformatics* **17**, 282–283 (2004).

703 9. Waterhouse, A. M., Procter, J. B., Martin, D. M. A., Clamp, M. & Barton, G. J. Jalview Version
704 2-A multiple sequence alignment editor and analysis workbench. *Bioinformatics* **25**, 1189–
705 1191 (2009).
706 10. Stamatakis, A. RAxML version 8: A tool for phylogenetic analysis and post-analysis of large
707 phylogenies. *Bioinformatics* **30**, 1312–1313 (2014).
708 11. Hodcroft, E. TreeCollapserCL4: Collapse Trees by Bootstrap. Available at:
709 http://emmahodcroft.com/TreeCollapseCL3.html.
710 12. Crooks, G., Hon, G., Chandonia, J. & Brenner, S. WebLogo: A Sequence Logo Generator.
711 *Genome Res* **14**, 1188–1190 (2004).
712 13. Mastronarde, D. N. Dual-axis tomography: An approach with alignment methods that preserve
713 resolution. *J. Struct. Biol.* **120**, 343–352 (1997).
714 14. Xiong, Q., Morphew, M. K., Schwartz, C. L., Hoenger, A. H. & Mastronarde, D. N. CTF
715 determination and correction for low dose tomographic tilt series. *J. Struct. Biol.* **168**, 378–387
716 (2009).
717 15. Castaño-Díez, D., Kudryashev, M., Arheit, M. & Stahlberg, H. Dynamo: A flexible, user-friendly
718 development tool for subtomogram averaging of cryo-EM data in high-performance computing
719 environments. *J. Struct. Biol.* **178**, 139–151 (2012).
720 16. Castaño-Díez, D., Kudryashev, M. & Stahlberg, H. Dynamo Catalogue: Geometrical tools and
721 data management for particle picking in subtomogram averaging of cryo-electron tomograms.
722 *J. Struct. Biol.* **197**, 135–144 (2017).
723 17. Kabsch, W. *et al. XDS*. *Acta Crystallogr. Sect. D Biol. Crystallogr.* **66**, 125–132 (2010).
724 18. Bibby, J., Keegan, R. M., Mayans, O., Winn, M. D. & Rigden, D. J. AMPLE: A cluster-and-
725 truncate approach to solve the crystal structures of small proteins using rapidly computed ab
726 initio models. *Acta Crystallogr. Sect. D Biol. Crystallogr.* **68**, 1622–1631 (2012).
727 19. Keegan, R. M. *et al.* Exploring the speed and performance of molecular replacement with
728 AMPLE using QUARK ab initio protein models. *Acta Crystallogr. Sect. D Biol. Crystallogr.* **71**,
729 338–343 (2015).
730 20. Thomas, J. M. H. *et al.* Routine phasing of coiled-coil protein crystal structures with AMPLE.
731 *IUCrJ* **2**, 198–206 (2015).
732 21. Adams, P. *et al.* The Phenix Software for Automated Determination of Macromolecular

733 Structures. *Methods* **292**, 342–351 (2009).

734 22. Emsley, P., Lohkamp, B., Scott, W. G. & Cowtan, K. Features and development of Coot. *Acta*
735 *Crystallogr. Sect. D Biol. Crystallogr.* **66**, 486–501 (2010).

736 23. Yao, Q. *et al.* Short FtsZ filaments can drive asymmetric cell envelope constriction at the onset
737 of bacterial cytokinesis. *EMBO J.* **36**, 1577–1589 (2017).

738 24. Schwede, T., Kopp, J., Guex, N. & Peitsch, M. C. SWISS-MODEL: An automated protein
739 homology-modeling server. *Nucleic Acids Res.* **31**, 3381–3385 (2003).

740

741
742
743
744

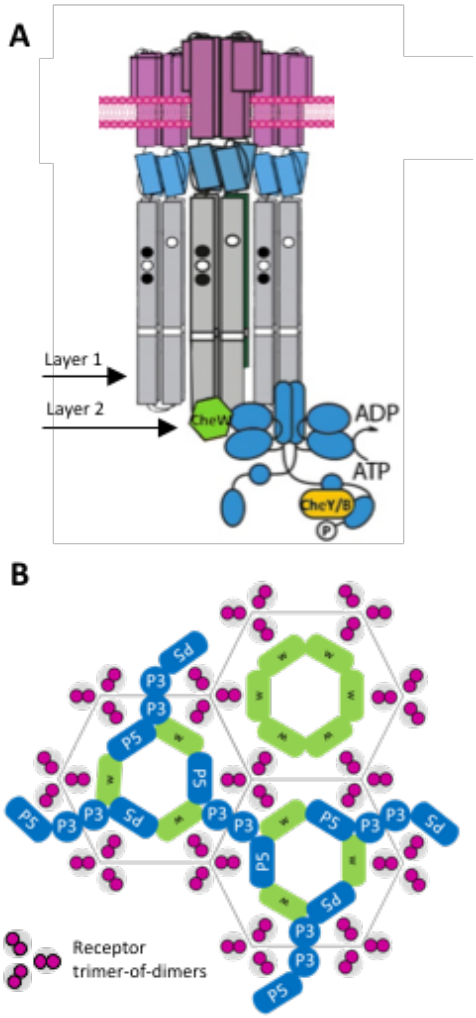

Fig. S1 The arrangement of the canonical chemoreceptor array, exemplified in *Escherichia coli* (*Ec*). (A) Transmembrane chemoreceptors form dimers that function as a trimer-of-dimers module to modulate the activity of the histidine kinase CheA (blue) via a coupling protein CheW (green). In cryo-ET experiments, cross-sections at Layer 1 reveals the arrangement of chemoreceptors and Layer 2 reveals the position of the kinase. (B) In all organisms investigated previously, CheA is integrated into the array with hexagonal (pseudo-P6) symmetry.

Fig. S2 The chemosensory class profile of Spirochaetota. Sequences belonging to the four major classes of Spirochaetota are marked: UBA4802 (dark red), Leptospira (purple), Brachyspirae (cyan), UBA6919 (blue), Brevinematia (yellow), GWE2-31-10 (green) and Spirochaetia (light green). Nodes are marked for presence of classes F1 (orange), F2 (red), F5 (blue), F7 (light green), F8 (green), ACF (light blue), and Tfp (purple). Genomes not present in MiST3 database are marked as grey. F2 systems with CheW-CheR$_{like}$ are marked with a black outline around the red circle.

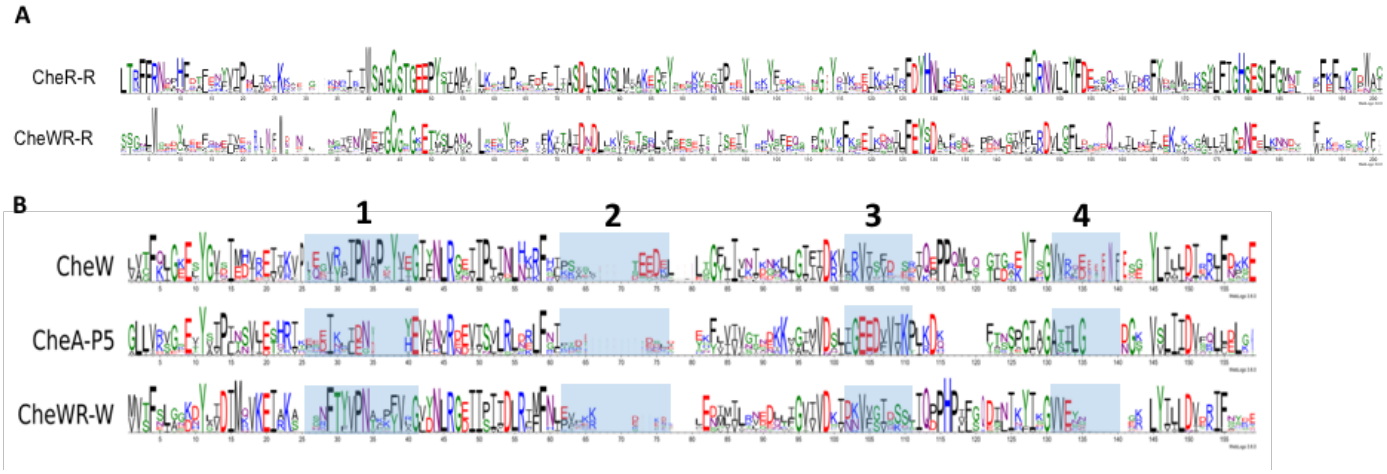

Fig. S3 (A) Sequence logo of representative sequences of the two groups of CheR-containing proteins in the F2 system. (B) Sequence logo of representative sequences of the three groups of CheW-containing proteins in the F2 system. Blue boxes denote the location of variable regions identified in the *Td* CheW and P5 homologs. In these locations, all regions possess unique conserved residues with the exception of Region 2, which is not at the CheA:CheW ring interfaces.

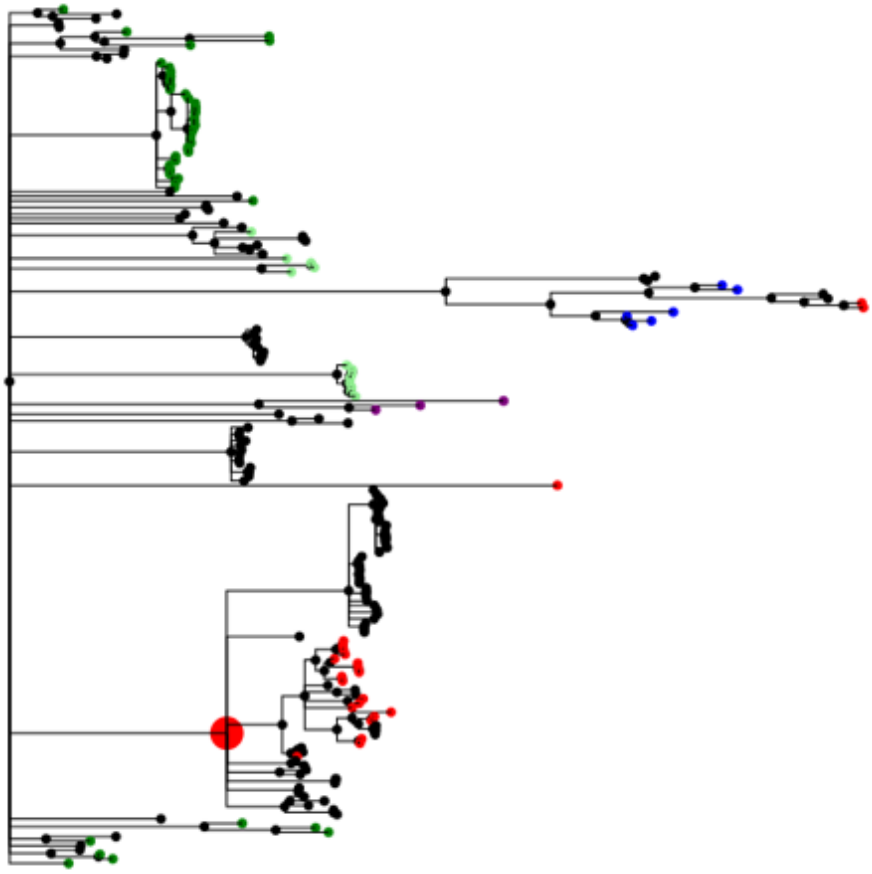

Fig. S4 Phylogenetic tree of CheW sequences in genomes with at least one CheA-F2 suggests a last common ancestor of CheW-F2 sequences. We mapped the sequences of CheW from the classes F2 (red), F5(purple), F7 (light green), F8 (green) and ACF (blue). The larger red internal node marks a candidate of the last common ancestor of CheW-F2.

A

Td strain	No. Cells/Arrays	No. Particles
WT	11	728
Δ2498	10	894
Δ2498Δ2496	10	554
ΔCheR$_{like}$	5	194

B

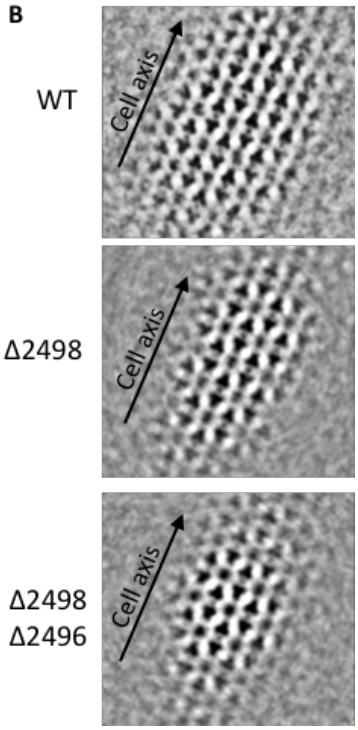

Fig. S5 (A) The number of arrays and particles selected to generate sub-tomogram averages for each *Td* strain. (B) Sub-tomogram averages reveal the orientation of the cell axis with respect to the orientation of the chemotaxis arrays. Intriguingly, the arrays have a preferred orientation in the cells and this orientation is conserved in WT and deletion mutants.

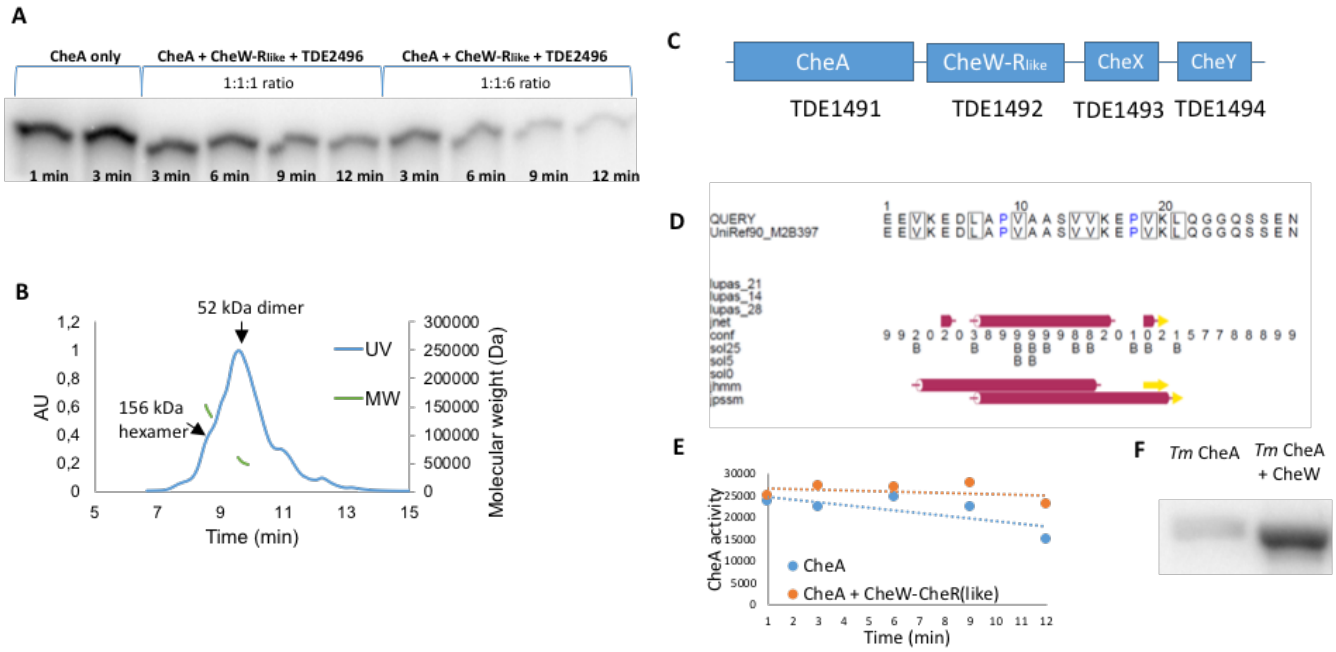

Fig. S6 (A) The soluble receptor TDE2496 deactivates *Td* CheA in a concentration-dependent manner. (B) MALS experiments demonstrate that TDE2496 forms the expected dimer (52 kDa) and hexamer (156 kDa) oligomeric states. (C) The CheW-CheR$_{like}$ protein is conserved on the same operon as the only CheA, CheX, and CheY proteins in *Td*. (D) The CheW-CheR$_{like}$ linker is predicted to forma single alpha helix flanked by unordered regions (Jpred). (E) Radioisotope assays that monitor CheA autophosphorylation over time in the presence and absence of CheW-CheR$_{like}$ demonstrate a difference in CheA activity. (F) In the *T. maritima* system, the presence of CheW also activates CheA kinase activity. Both samples are at time point 3 minutes.

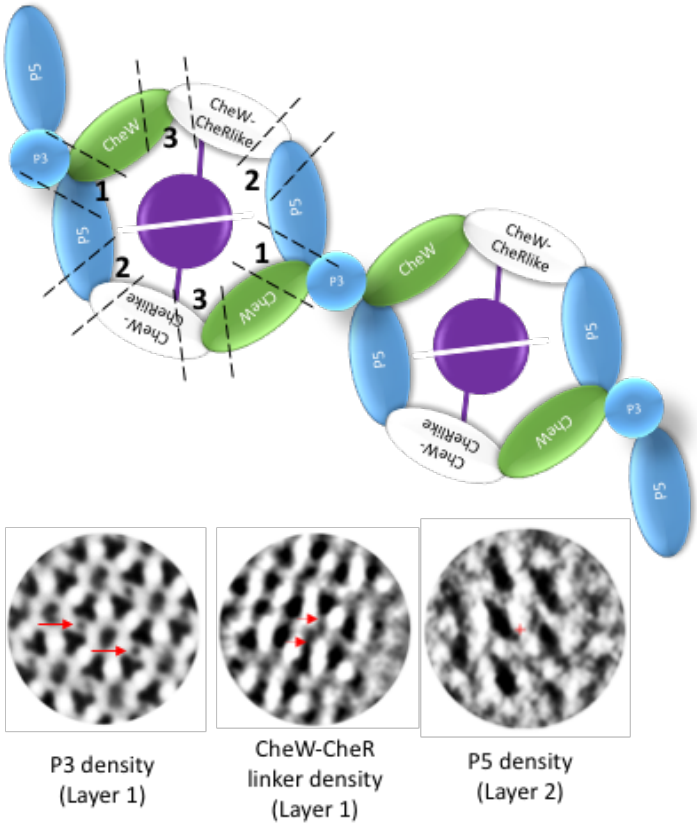

Fig. S7 The arrangement of chemotaxis CheA:CheW rings in *Td.* Top: The CheA:CheW rings consists of three domains: CheA P5 (blue), a classical CheW protein (green), and the CheW domain of CheW-CheR$_{like}$ (white). Three unique interfaces are produced and the CheR$_{like}$ domain (purple) extends to the center of the rings to interact with one another. Bottom: The location of the CheW-CheR$_{like}$ protein in the rings is evident by examining the location of the CheA domains with respect to the CheW-CheR$_{like}$ linker.

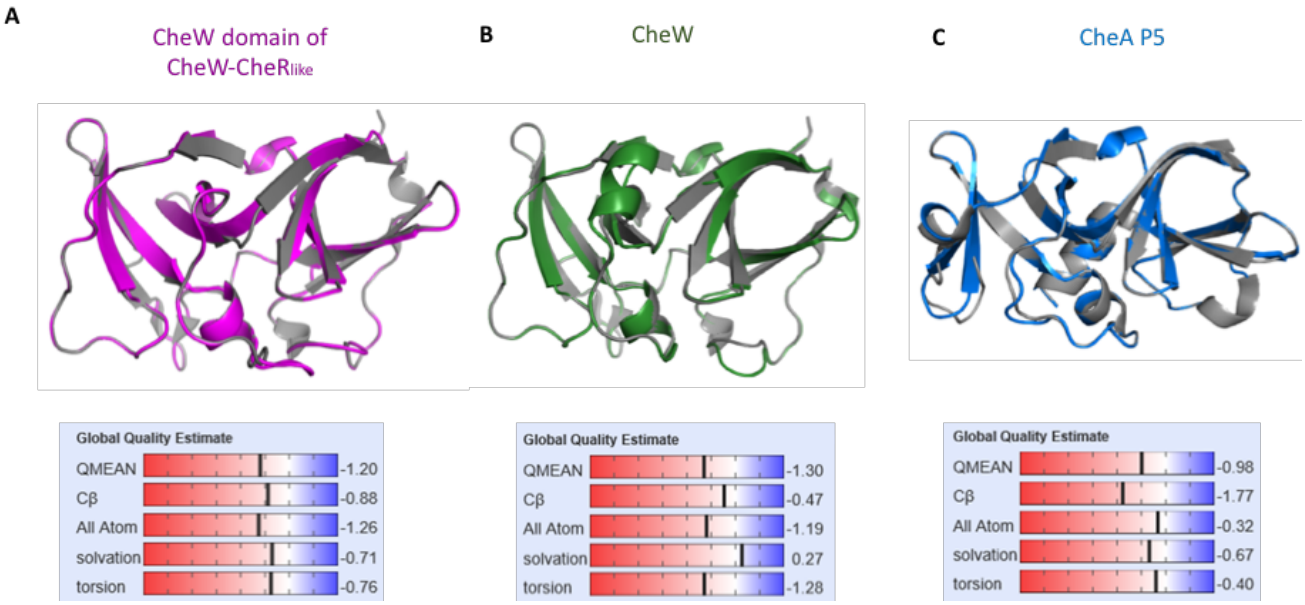

Fig. S8 Homology models of *Td* CheW domains and CheA P5. (A) A homology model of the CheW domain of CheW-CheRlike using *Thermoanaerobacter tengcongensis* (*Tt)* CheW (PDB ID: 2QDL) as the template. (B) A homology model of the classical *Td* CheW using *Tt* CheW (PDB ID: 2QDL) as the template. (C) A homology model of CheA P5 using *E. coli* CheA P5 (PDB ID: 6S1K) as the template.

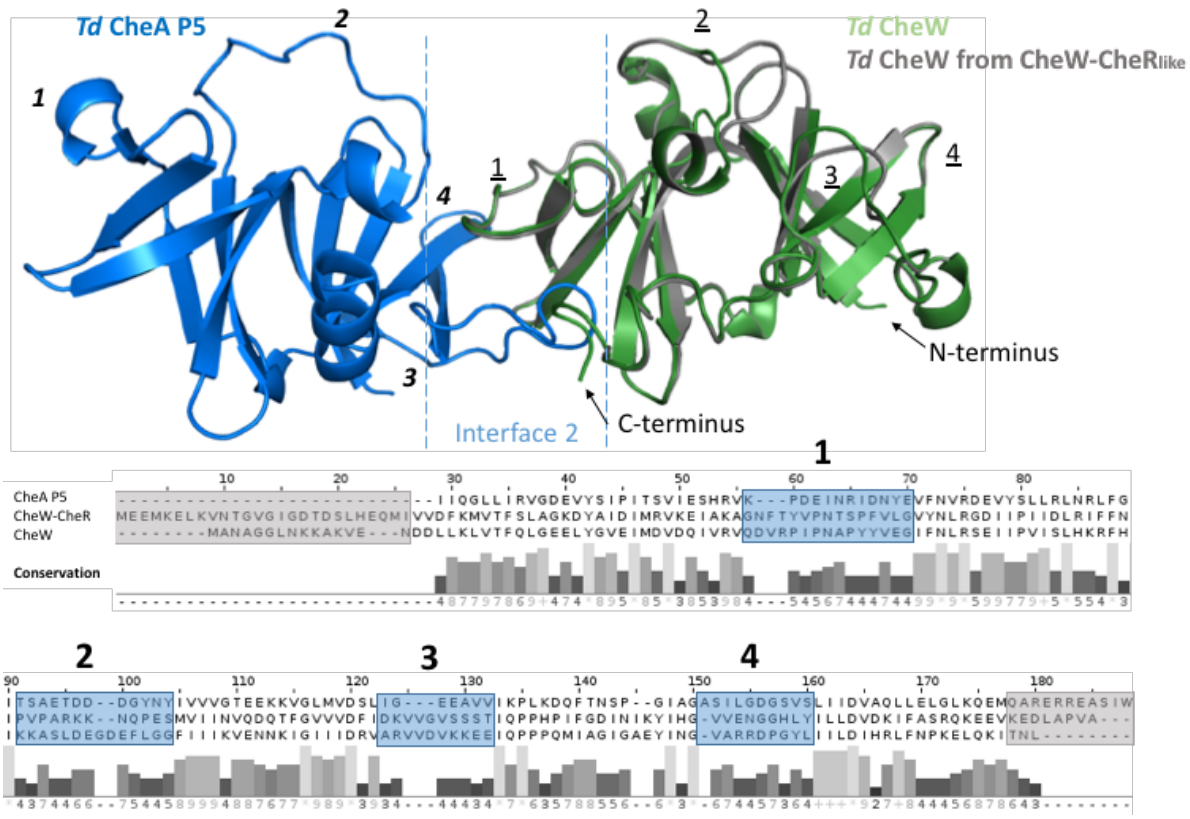

Fig. S9 Homology models of *Td* CheA P5, CheW, and the CheW domain of CheW-CheR$_{like}$ mapped onto a previously determined crystal structure of *Thermotoga maritima* CheA P5 and CheW (PDB ID: 3UR1). Variable regions between the three domains (blue boxes) were determined by sequence alignments of the three domains followed by conservation analysis. These variable regions are located at the rings interface regions. The CheW domains also have variable N-terminal and C-terminal regions that are not complimented in P5 (grey boxes). Variable regions for P5 and the CheW domains are denoted on the homology models by italicized numbers and underlined numbers, respectively.

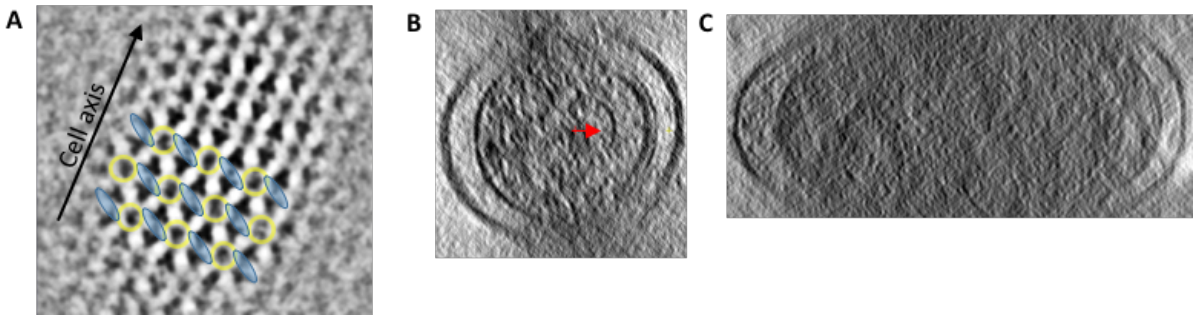

Fig. S10 (A) Sub-tomogram averaging of *Td* WT and mutant strains reveal that linked CheA:CheW rings (yellow) run perpendicular to the cell axis via a strict linear orientation of CheA (blue). Averages from WT *Td* are illustrated here but apply to all strains. (B) The curvature of the inner membrane of *Td* at chemotaxis arrays in the reconstructions is 35.8 +/- 6.6 /µm (270 Å radius). The curvature of the CheA:CheW baseplate (red arrow) is 65.6 +/- 19 /µm (152 Å radius). (C) *V. cholerae* minicells have an inner membrane curvature of 9.15 +/- 4.5 /µm (radius 1092 Å).

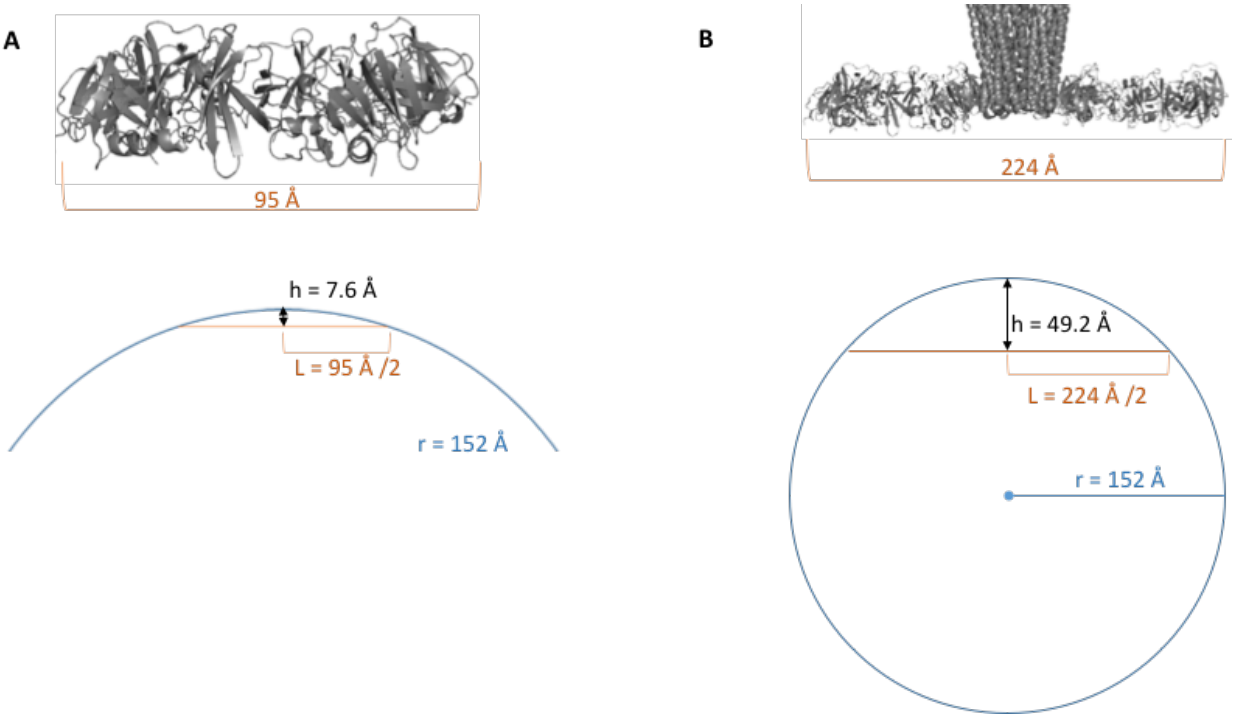

Fig. S11 Modeling of CheA:CheW rings to the curvature of the *Td* baseplate. (A) For single CheA:CheW rings to follow the baseplate curvature, it must buckle by an average of 7.6 Å toward the membrane. (B) In order for two linked CheA:CheW rings to run perpendicular to the cell axis, the center of the rings (P3) must buckle by 49.2 Å toward the cell membrane.

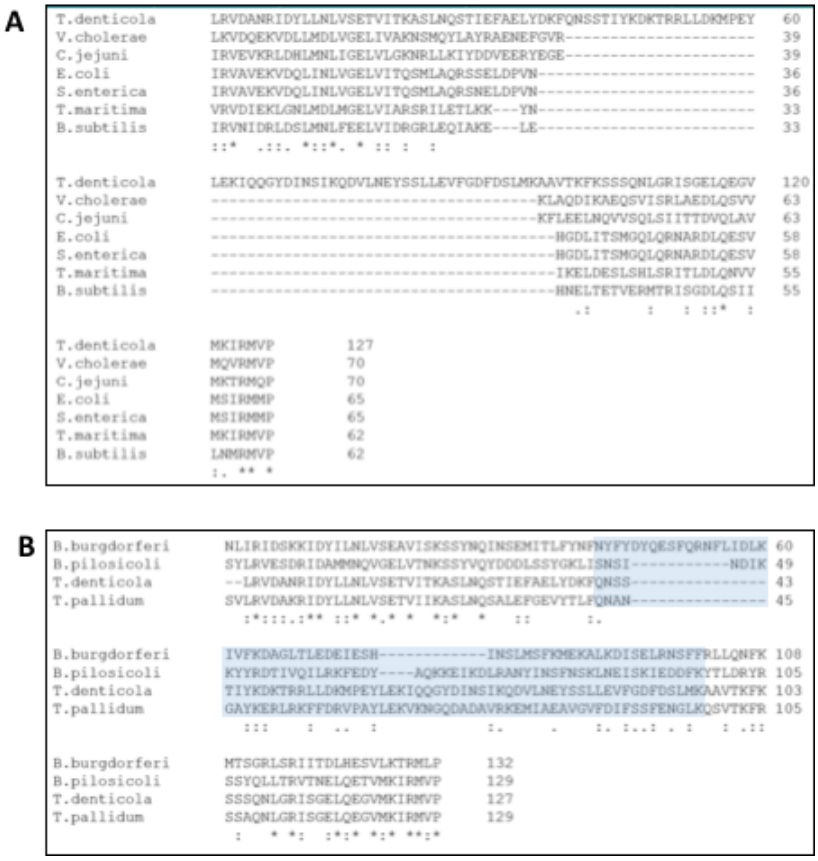

Fig. S12 Multiple sequence alignments of the CheA P3 domain from several bacteria demonstrates the presence of additional P3 residues in *Td* and other Spirochetes. (A) CheA P3 alignments of *Td* and P3 from other bacteria with previously characterized chemotaxis proteins. *Td* possesses ~50 residues that are not found in the other homologs and are located in between the traditional dimerization helices. (B) *Td* CheA P3 aligned with other Spirochete P3. The additional residues identified in alignment **A** are highlighted in blue. Figures were made using Clustal Omega.

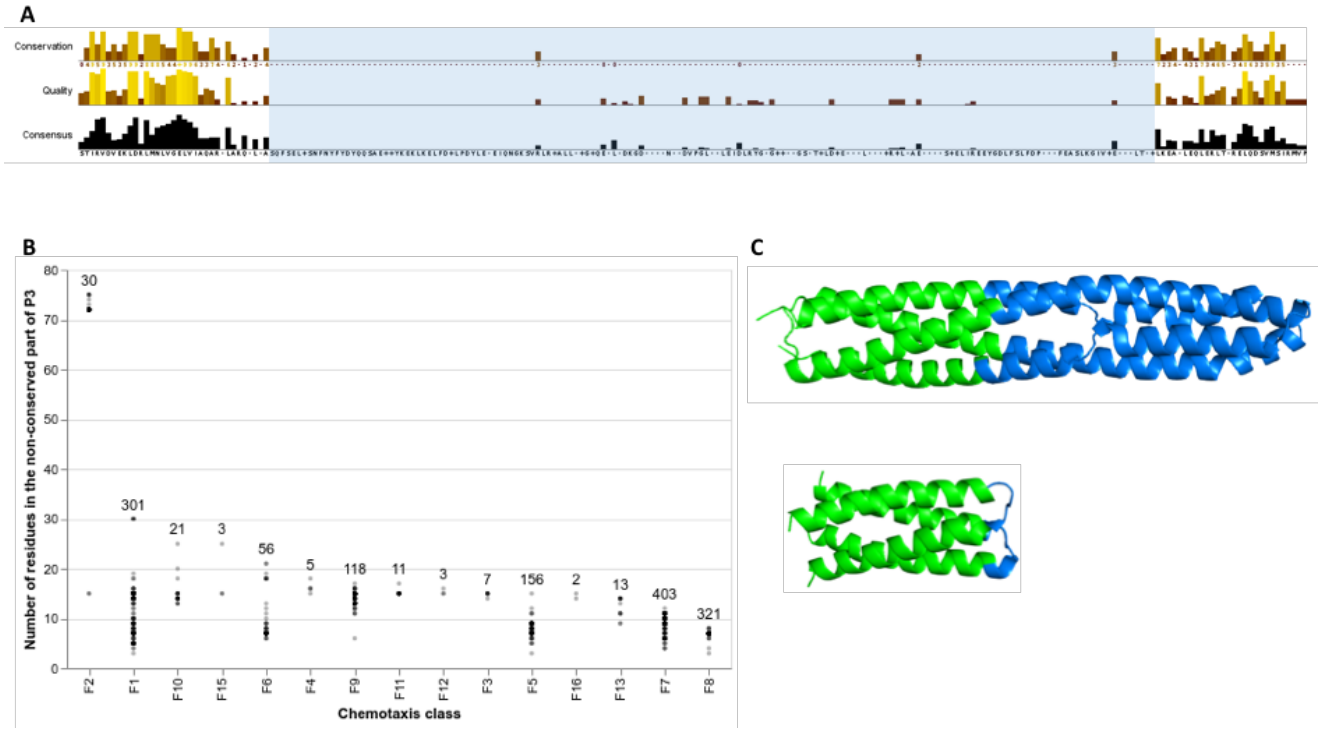

Fig. S13 Analysis of non-redundant CheA P3 domains with a 75% sequence identity cut-off (1450 sequences). (A) Conservation scores of the P3 alignment with the 1450 sequences. The traditional P3 helices are largely conserved, but regions located between the helices are non-conserved. (B) Analyses of CheA from different chemotaxis classes reveals that CheA F2 homologs possess the most residues in the non-conserved region of P3. (C) The non-conserved regions are llustrated with the two known CheA P3 structures. Top: *Td* P3 possesses 71 residues that align to the non-conserved region (PDB ID: 6Y1Y). Bottom: *Tm* P3 possesses seven residues that align to the non-conserved region (PDB ID: 1B3Q).

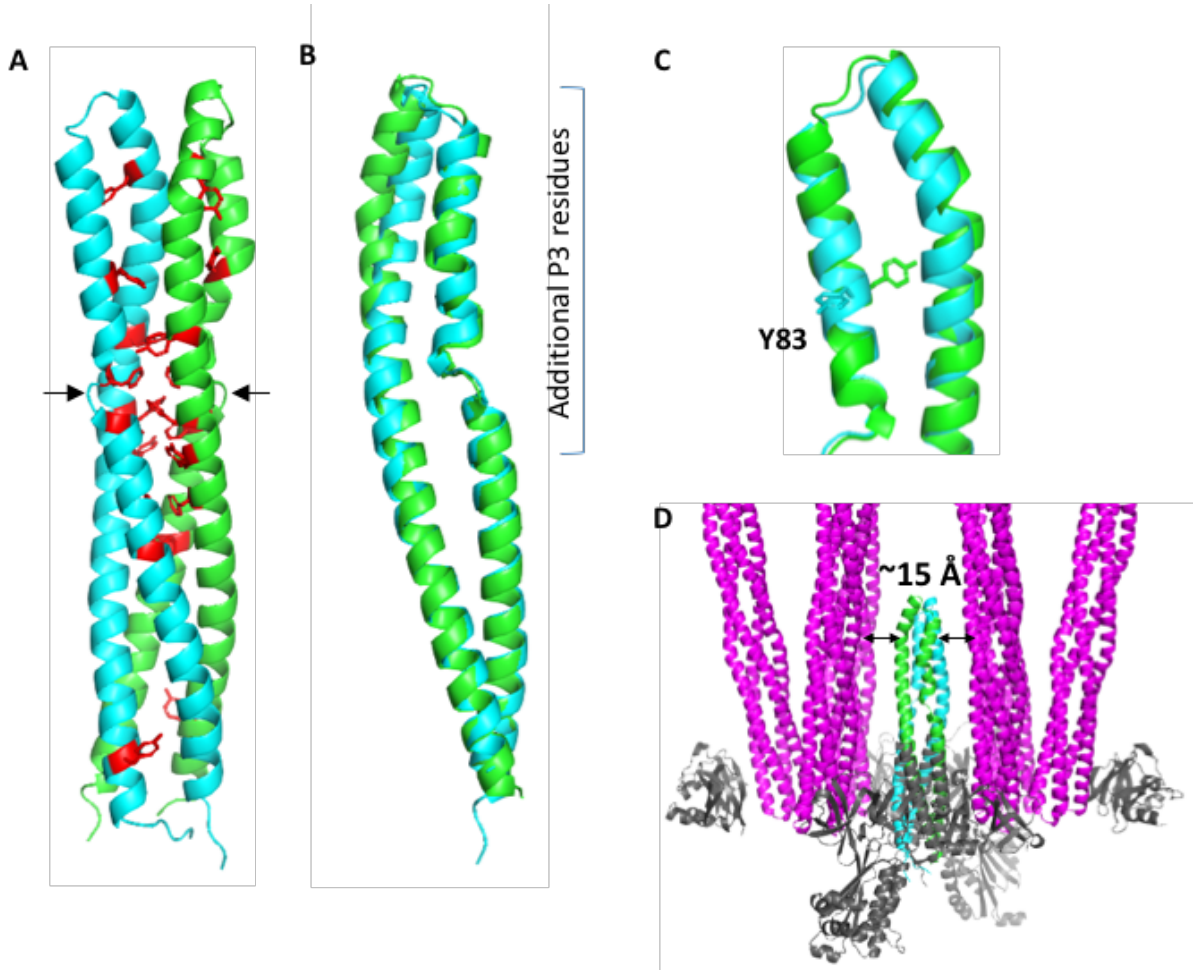

Fig. S14 The P3 domain of *Td* CheA. (A) The CheA P3 dimer contains a cluster of Phe and Tyr residues near the breakages in the helices (black arrows). All Phe and Tyr residues are highlighted in red. (B) The crystal structure of CheA P3 demonstrates asymmetry in the subunits. (C) Repositioning of Y82 in the subunits induces alterations of adjacent residues and may account for subunit asymmetry. (D) Alignment of the P3 structure to a previously determined model of the chemotaxis array in *E. coli* (PDB ID: 3JA6) indicates that the P3 domain lies within ~15 Å of the receptors (when measuring from peptide back-bone). CheA and CheW in this model are shown in grey.

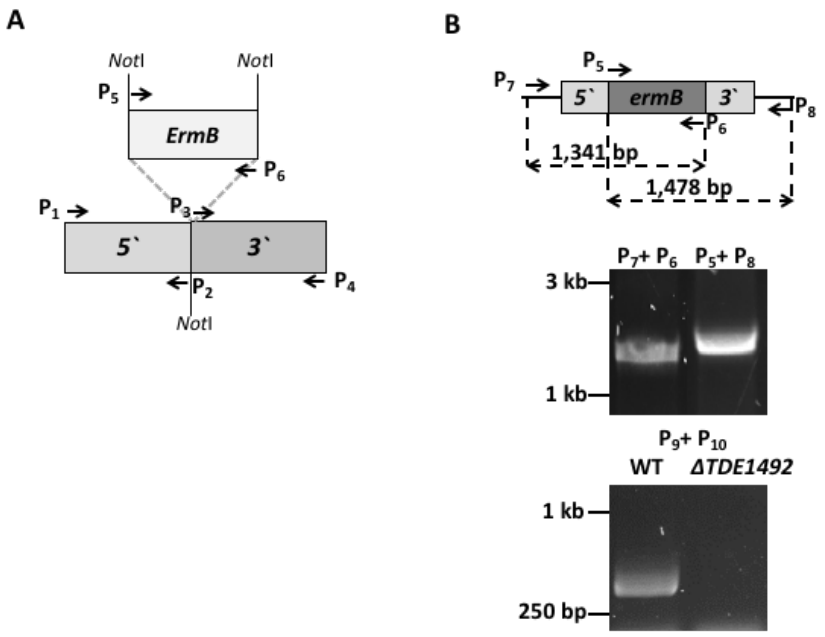

Fig. S15 Diagrams illustrating construction of the *TDE1492::ermB* vector (A) for the targeted mutagenesis of *TDE1492 (781-1,308 nt)* by in-frame replacement of *TDE1492* using *ermB* cassette**.** These constructs were constructed by two-step PCR followed by DNA cloning. Arrows represent the relative positions and orientations of these primers, which are listed in Table S3. *ermB* = erythromycin resistance. (B) Characterization of the *ΔTDE1492* strain by PCR analysis. The top panel illustrates how the PCR analysis is designed; the bottom panel is the PCR results. Arrows represent the relative positions and orientations of these primers; the numbers are predicted sizes of PCR products generated by the corresponding primers. The primer P_7 is located at the 5'-end of *TDE1492*, P_6 at the 3'-end of *ermB*, P_5 at the 5'-end of *ermB*, P_8 at the flanking region of *TDE1492*, P_9 at the middle of *TDE1492*, and P_{10} at the 3'- end of *TDE1492*. The sequences of these primers are listed in Table S3.

Fig. S16 Flowchart of the three major pipelines used to produce the bioinformatics datasets. Steps marked in red represents fetching information from MiST3 database, in green are steps requiring RegArch as a filter, and in blue indicate writing data to file.

Td strain	Average angle (°)
WT (n=9)	9.67 +/- 9.21
Δ2498 (n=9)	9.55 +/- 8.75
Δ2498Δ2496 (n=8)	12.18 +/- 7.62
Combined average:	**10.40 +/- 8.59**

Table S1A. Statistics for the average angle between the *Td* cell axis and the 'strands' of CheA:CheW rings.

Vc cell number	Inner membrane curvature (/μm)
1	6.2
2	15.4
3	14.2
4	7.4
5	4.3
6	7.5
Average:	**9.155 +/- 4.53**

Table S1B. Statistics of inner membrane curvature for 6 *Vc* mini-cells.

Td cell number	Inner membrane curvature (/µm)	Baseplate curvature (/µm)
1	35.0	49.7
2	25.4	54.0
3	34.2	63.7
4	43.1	96.1
5	30.8	99.7
6	41.1	55.7
7	39.6	74.6
8	33.1	47.7
9	46.2	47.8
10	29.1	67.1
Average:	**35.8 +/- 6.6**	**65.6 +/- 19**

Table S1C. Statistics of inner membrane and baseplate curvature for 10 WT *Td* cells.

	***Td* P3 domain (PDB: 6Y1Y)**
Wavelength	0.979100
Resolution range	75.36 – 1.50 (1.55 – 1.50)
Space group	C 1 2 1
Unit cell	a, b, c: 101.64, 28.77, 82.90 α, β, γ: 90, 114.75, 90
Total reflections	53542
Unique reflections	35178 (3490)
Multiplicity	6.9 (6.2)
Completeness (%)	96.72 (99.31)
Mean I/sigma(I)	14.7 (5.4)
R-merge	0.063(0.290)
R-meas	0.075(0.350)
R-pim	0.040(0.193)
CC1/2	0.99(0.94)
Reflections for refinement	33864 (3361)
Reflections for R-free	1308 (143)
R-work	0.187 (0.205)
R-free	0.211 (0.244)
No. non-H atoms	2344
macromolecules	2028
ligands	0
solvent	316
Protein residues	253
RMS(bonds)	0.006
RMS(angles)	0.93
Ramachandran favored (%)	100
Ramachandran allowed (%)	0.00
Ramachandran outliers (%)	0.00
Rotamer outliers (%)	0.00
Clashscore	6.87
Average B-factor	19.1
macromolecules	17.2
solvent	28.2

905
906 **Table S2.** Data collection and refinement statistics for *Td* CheA P3 domain.
907
908
909
910

Primers	Sequences (5'-3')	Note [a]
P_1	CGGGCGTAGGCATCGGAGATAC	5` portion for TDE1492 inactivation; [F]
P_2	TTACAATATCACCTGAGCTGGCGGCCGCTTAAGGTGACAAGAAAGATGATA	5` portion for TDE1492 inactivation; [R]
P_3	TATCATCTTTCTTGTCACCTTAAGCGGCCGCCAGCTCAGGTGATATTGTAA	3` portion for TDE1492 inactivation; [F]
P_4	CCCAGAGCACTTATCATAAC	3` portion for TDE1492 inactivation; [R]
P_5	ATGAACAAAAATATAAAATATTCTC	Erythromycin B cassette (ermB); [F]
P_6	TTATTTCCTCCCGTTAAATAATAG	Erythromycin B cassette (ermB); [R]
P_7	ATGGAAGAAATGAAAGAAC	5` flanking region of TDE1492, ΔTDE1492 PCR analysis; [F]
P_8	GATATAGTTCTTGGCTCCAAG	3` flanking region of TDE1492, ΔTDE1492 PCR analysis; [R]
P_9	GAGGCCTATATAAATGCC	TDE1492, ΔTDE1492 PCR analysis; [F]
P_{10}	CTTGGGCATTGCCTCATTATG	TDE1492, ΔTDE1492 PCR analysis; [R]

Table S3. Oligonucleotide primers used in this study

[a] Underlined sequences are engineered restriction cut sites for DNA cloning; [F] forward; [R] reverse.

911
912
913
914
915